Ocean Science

Interannual variability of sea level in the southern Indian Ocean: local vs. remote forcing mechanisms

Marion Kersalé[1,2], **Denis L. Volkov**[1,2], **Kandaga Pujiana**[1,2], and **Hong Zhang**[3]

[1]Cooperative Institute for Marine and Atmospheric Studies, University of Miami, Miami, Florida, USA
[2]NOAA Atlantic Oceanographic and Meteorological Laboratory, Miami, Florida, USA
[3]Jet Propulsion Laboratory, California Institute of Technology, Pasadena, California, USA

**Correspondence:** Marion Kersalé (marion.kersale@gmail.com)

Abstract. The subtropical southern Indian Ocean (SIO) has been described as one of the world's largest heat accumulators due to its remarkable warming during the past 2 decades. However, the relative contributions of remote (of Pacific origin) forcing and local wind forcing to the variability of heat content and sea level in the SIO have not been fully attributed. Here, we combine a general circulation model, an analytic linear reduced-gravity model, and observations to disentangle the spatial and temporal inputs of each forcing component on interannual to decadal timescales. A sensitivity experiment is conducted with artificially closed Indonesian straits to physically isolate the Indian Ocean and Pacific Ocean, intentionally removing the Indonesian Throughflow (ITF) influence on the Indian Ocean heat content and sea level variability. We show that the relative contribution of the signals originating in the equatorial Pacific vs. signals caused by local wind forcing to the interannual variability of sea level and heat content in the SIO is dependent on location within the basin (low latitude vs. midlatitude and western side vs. eastern side of the basin). The closure of the ITF in the numerical experiment reduces the amplitude of interannual-to-decadal sea level changes compared to the simulation with a realistic ITF. However, the spatial and temporal evolution of sea level patterns in the two simulations remain similar and correlated with El Niño–Southern Oscillation (ENSO). This suggests that these patterns are mostly determined by local wind forcing and oceanic processes, linked to ENSO via the "atmospheric bridge" effect. We conclude that local wind forcing is an important driver for the interannual changes of sea level, heat content, and meridional transports in the SIO subtropical gyre, while oceanic signals originating in the Pacific amplify locally forced signals.

1 Introduction

The Indian Ocean has been characterized as one of the major heat accumulators in the ocean with a significant increase of ocean heat content (OHC) and sea level during the past 2 decades, in particular in the subtropical southern Indian Ocean (SIO) (Roemmich et al., 2015; Nieves et al., 2015; Volkov et al., 2017; Y. Zhang et al., 2018; Ummenhofer et al., 2020) (Fig. 1a). Heat accumulation in the SIO has resulted in the acceleration of regional sea level rise (Jyoti et al., 2019), more frequent and intense marine heat waves (Oliver et al., 2018), impacts on Indian summer monsoon rainfall (Venugopal et al., 2018; Gao et al., 2018), and increased inter-ocean heat transport via the Agulhas leakage (Wang, 2019). Understanding the mechanisms of the regional sea level and heat content variability is, therefore, necessary for improving regional weather and climate forecasts (Levitus et al., 2005; Church and White, 2011; IPCC, 2021).

The decade-long increase of the upper-ocean heat content in the SIO in 2005–2013 (Fig. 1a) has been attributed to an enhanced heat transport from the equatorial western Pacific carried by the Indonesian Throughflow (ITF; Lee et al., 2015). The ITF is driven by the inter-ocean pressure gradient that exists between the western equatorial Pacific Ocean and the eastern Indian Ocean (Wyrtki, 1987) and serves as an important component of the global thermohaline circulation (Gordon, 1986; Sloyan and Rintoul, 2001; Sprintall et al.,
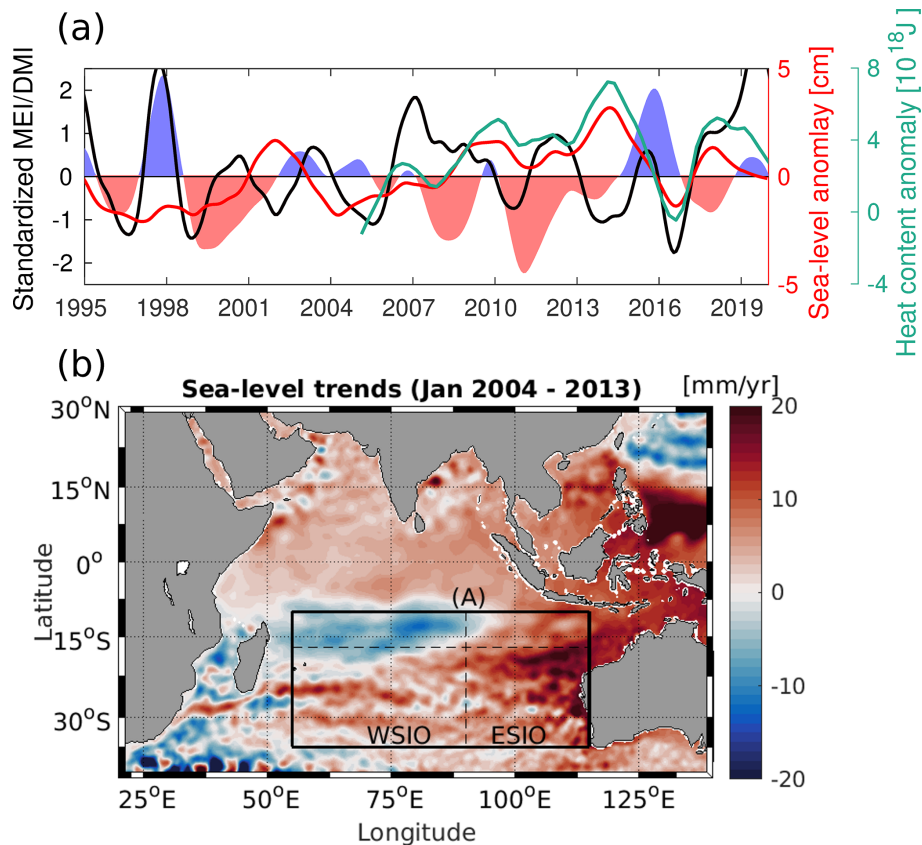
Figure 1. Climate indices vs. sea level and heat content changes. **(a)** Time series of the monthly standardized MEI (El Niño and La Niña are shown by blue and red shading, respectively) and DMI index (black line). Monthly sea level anomaly (SLA) from altimetry (red line) and seasonal heat content anomaly from 0 to 2000 m depth (green line) from World Ocean Database (Levitus et al., 2012) are also represented, both averaged over 55–115° E and 10–30° S (box A in **b**). All the time series are low-pass filtered with a cutoff period of 1 year. **(b)** Dynamic sea level trends in 2004–2013 (global mean sea level is subtracted). Boxes in **(b)** mark the distinction between the tropics vs. subtropics and eastern vs. western SIO regimes.

2014). With a time-mean volume transport of about 15 sverdrups ($1\,Sv = 10^6\,m^3\,s^{-1}$; Sprintall et al., 2009), the ITF experiences substantial interannual variations linked to the El Niño–Southern Oscillation (ENSO; Meyers, 1996; England and Huang, 2005). ENSO is characterized by alternating positive (El Niño) and negative (La Niña) anomalies in the upper OHC in the eastern equatorial Pacific, as demonstrated by the Multivariate ENSO Index (MEI, shown as blue and red shading in Fig. 1a). These anomalies eventually impact the SIO by modulating the ITF volume and heat transport – the so-called "ocean tunnel" effect (Lee et al., 2015; Y. Zhang et al., 2018; Gordon et al., 2019; Volkov et al., 2020). La Niña conditions favor a stronger ITF, while El Niño conditions are associated with a weaker ITF (Gordon et al., 1999; Sprintall and Revelard, 2014). The majority of the ITF water flows westward with the South Equatorial Current (SEC) between 10–20° S, while part of the ITF makes its way to the southward-flowing Leeuwin Current (LC) off the western Australian coast (Thompson, 1984; Domingues et al., 2007). Temperature anomalies carried by the ITF into the SIO can

also propagate along the western Australian coast southward as coastally trapped waves (Clarke, 1991; Clarke and Liu, 1994; Wijffels and Meyers, 2004).

Effects of the ITF on the circulation and thermal structure of the Indian Ocean were investigated by comparing solutions of an ocean general circulation model with open and closed Indonesian passages in previous studies (e.g., Hughes et al., 1992; Lee et al., 2002; Song and Gordon, 2004). These studies focused on seasonal to interannual variability and showed that the ITF warms the upper Indian Ocean and deepens its thermocline. Subsequently, the full role of the ITF was analyzed with coupled general circulation models (e.g., Wajsowicz and Schneider, 2001; Song et al., 2007). The changes were similar to those reported by ocean-only model experiments but with larger amplitudes. In addition, they showed that the closure of the ITF significantly increased the interannual variability in the eastern tropical Indian Ocean (Song et al., 2007). Closing the ITF shoals the eastern tropical Indian Ocean thermocline (Lee et al., 2002; Song et al.,

2007), resulting in greater cooling episodes due to enhanced atmosphere–thermocline coupled feedback.

Besides the ocean tunnel effect, the variability of sea level and OHC in the SIO is also driven by local atmospheric forcing. Wind-driven ocean dynamics are the dominant contributor of the upper-ocean temperature variability in the equatorial Indian Ocean (Yuan et al., 2020). Wind stress curl induces Ekman pumping, and alongshore winds cause coastal upwelling and downwelling. These processes alter the depth of the thermocline and therefore drive regional changes in sea level and OHC. Wind forcing over the SIO is related to ENSO due to atmospheric teleconnections via the Walker circulation (Schott et al., 2009). The wind-driven changes of sea level and OHC in the Indian Ocean associated with ENSO are often referred to as the "atmospheric bridge" effect (e.g., Volkov et al., 2020). The atmospheric bridge acts mostly through changes in trade and equatorial winds. Equatorial wind anomalies generate differences in sea surface temperature (SST) anomalies between the western and eastern equatorial Indian Ocean, termed the Indian Ocean Dipole (IOD; Saji and Yamagata, 2003) and represented by the Dipole Mode Index (DMI; black line in Fig. 1a). The IOD impacts sea level and heat content in the SIO through changes in the thermocline depth to the west and south of Sumatra and Java, which can also modulate the ITF transport (Sprintall et al., 2009; Drushka et al., 2010; Lu et al., 2018; Pujiana et al., 2019). Although sometimes ENSO and IOD are regarded as a single entity (Allan et al., 2001), there is more evidence that the two processes are independent from each other (Ashok et al., 2003). Finally, the Southern Annular Mode (SAM) was diagnosed as the ultimate large-scale climatic forcing over the SIO (Schott et al., 2009). The SAM has significant effects on the supergyre, which links all the three subtropical gyres of the Southern Hemisphere (Cai et al., 2005; Ridgway and Dunn, 2007). SAM further contributes to modulating the teleconnections between ENSO and IOD by enhancing sea surface temperature (SST) gradients within the SIO (Cleverly et al., 2016).

The signals of Pacific origin that enter the SIO with the ITF and reach the western Australian coast radiate westward as eddies and Rossby waves (Cai et al., 2005; Zhuang et al., 2013; Zheng et al., 2018). This process is hereafter referred to as remote or eastern boundary forcing. On seasonal to interannual timescales, local wind forcing and related Ekman pumping over the ocean interior can also generate oceanic Rossby waves and/or alter those emanating from the eastern boundary (Masumoto and Meyers, 1998; Birol and Morrow, 2001). Menezes and Vianna (2019) found that the westward propagation observed in the eastern SIO (ESIO – Fig. 1b) basin and in the western SIO (WSIO – Fig. 1b) basin reveals a superposition of Rossby waves generated by processes near the eastern boundary on top of Rossby waves generated by Ekman pumping in the mid-basin. Thus, westward propagation provides the primary mechanism for both the ocean tunnel and the atmospheric bridge effects to transfer energy and

seawater properties across the entire SIO (Morrow and Birol, 1998)

On the basis of satellite altimetry, previous studies have examined the relative importance of the eastern boundary and local wind forcing on the interannual variability of sea level and heat content in the SIO. Volkov et al. (2020) showed that the signals of the Pacific origin dominate sea level variability in the ESIO, while the local wind-induced variability is more influential in the WSIO, indicating a dependence on longitude. They also noted that the relative importance of local and remote drivers in the WSIO is time dependent: in some periods remote and local forcing mechanisms appear to have similar magnitudes, while in other periods local wind forcing may become dominant. The latter happened in 2016–2018 when the OHC and sea level in the SIO recovered after an abrupt drop associated with the 2014–2016 El Niño (Fig. 1a). Nagura and McPhaden (2021) extended the analysis of the eastern boundary and local wind forcing mechanisms by also demonstrating a latitudinal dependence. They confirmed that the influence of the eastern boundary forcing is confined to the ESIO but only at low latitudes (from 10 to 17° S). Between 10 and 35° S, they identified two regimes: one in the tropics where local forcing has a bigger effect, and another in the midlatitudes (subtropics) where remote forcing has a greater influence. These results are in agreement with earlier studies that suggested the dominance of local wind forcing in driving sea level variability at low latitudes (from 11 to 13° S – Masumoto and Meyers, 1998; Zhuang et al., 2013), and the prevalence of variability radiated from the eastern boundary at midlatitudes (from 20 to 25° S – Zhuang et al., 2013; Menezes and Vianna, 2019).

It is usually assumed that the interannual variability of OHC and sea level along the western Australian coast is strongly linked to remote wind forcing in the tropical Pacific and therefore represents the ocean tunnel effect (e.g., Nagura and McPhaden, 2021, and references therein). However, the impact of the alongshore wind forcing that also drives sea level variability along the coast is often disregarded. The alongshore winds are part of the large-scale atmospheric circulation over the SIO dominated by southeasterly trade winds, the variability of which is modulated by ENSO via the atmospheric bridge effect.

The objective of this study is to revisit the question of the interplay between the remote and local drivers of the interannual-to-decadal sea level variability in the SIO with a different approach. Previous studies of sea level variability in the SIO were mainly based on simple linear models (e.g., Zhuang et al., 2013; Jin et al., 2018; Menezes and Vianna, 2019; Volkov et al., 2020; Nagura and McPhaden, 2021). Although these models contain the essential dynamics capable of explaining the majority of the observed sea level variations, they adopt some assumptions and arbitrary parameters. Here, we aim to further investigate this topic using an ocean general circulation model that contains the full range of oceanic dynamical processes responsible for sea level vari-

ability. Specifically, we perform an ocean model sensitivity experiment in which we physically isolate the Indian Ocean and the Pacific Ocean by closing the Indonesian straits, thus artificially removing the ITF (ocean tunnel) influence on the Indian OHC and sea level variability. In this experiment, any variability observed along the SIO eastern boundary is primarily due to local forcing by constructs. We compare the results of this experiment with those from a realistic simulation with open Indonesian passages. This allows us to better quantify the relative contributions of the remote and local drivers. In addition, numerical simulations are combined with a linear reduced-gravity model and observations to disentangle the spatial and temporal dominance of each forcing component. Furthermore, we investigate in more detail the pronounced warming and the abrupt cooling observed in the SIO subtropical gyre in 2004–2013 and in 2014–2016, respectively (Fig. 1a). Finally, we explore how the interior meridional transports across the SIO are related to sea level variability.

2   Materials and methods

2.1   Ocean model

The ocean model used in this study is a global ocean and sea ice state estimate based on the Massachusetts Institute of Technology General Circulation Model (MITgcm, Marshall et al., 1998) and produced by the Estimating the Circulation and Climate of the Ocean (ECCO) consortium (https://ecco-group.org, last access: 5 February 2022). The ECCO consortium aims to create accurate, physically consistent, time-evolving estimates of ocean circulation by combining MITgcm with selected in situ and satellite observations (Menemenlis et al., 2005; Wunsch and Heimbach, 2007, 2013; Forget et al., 2015; Fukumori et al., 2017). The estimate uses the adjoint method to iteratively minimize the squared sum of weighted model–data misfits and to adjust the model control parameters (Wunsch et al., 2009; Wunsch and Heimbach, 2013). The data constraints include temperature and salinity profiles (from Argo floats, conductivity–temperature–depth (CTD), expendable bathythermograph (XBT), and ice-tethered profilers), satellite altimetry and gravimetry measurements, sea surface temperature fields from passive microwave radiometry, and satellite observations of sea ice concentration. The control parameters include the initial temperature and salinity fields, the 3D parameters of Gent–McWilliams and Redi mixing scheme (Redi, 1982; Gent and McWilliams, 1990), and the time-varying atmospheric boundary conditions. The ECCO solutions are then obtained by forward unconstrained model integrations using the optimized control parameters.

The modern generation of ECCO models employs a so-called lat–long–cap (LLC) grid, including LLC90 ($\sim 1°$), LLC270 ($\sim 1/3°$), and LLC4320 ($\sim 1/48°$), which allows

for an improved representation of the Arctic (no polar singularity and a fine grid for small deformation radius). The LLC grid has five faces covering the whole globe, with a simple, locally isotropic latitude–longitude grid between 70° S and 57° N and an Arctic cap (Forget et al., 2015). In this study, we use the ECCO LLC270 configuration (Y. Zhang et al., 2018), which provides a better representation of mesoscale variability compared to the latest ECCO LLC90 release (ECCO-V4r4, Forget et al., 2015). The horizontal resolution of the LLC270 grid varies spatially from 12 km at high latitudes to 28 km at midlatitudes. The vertical grid has 50 vertical layers, with the spacing increasing from 10 m near the surface to 457 m near the maximum model depth set to 6145 m.

The ECCO LLC270 solutions used in this study were obtained by free forward model integrations from January 1992 to June 2018 using the optimized control parameters and forced by the adjusted ERA-Interim atmospheric fields (Dee et al., 2011). To separate the influence of the Pacific Ocean on the variability of sea level and OHC in the Indian Ocean, we performed a numerical experiment with artificially closed Indonesian passages and the Torres Strait between Australia and New Guinea. The closure of the Indonesian passages was achieved by modifying the model bathymetry (Fig. 2a). To distinguish between the optimized, realistic model run with open Indonesian passages and the experiment with closed Indonesian passages, we refer to them hereafter as the "ITF-on" and the "ITF-off" experiments, respectively. It should be noted that the ITF-off experiment was run twice. The first run was performed to let the model reach a stable state. The second run was initialized using the output of the first run in January 2018, and the model was integrated again from January 1992 to June 2018. From now on, the ITF-off experiment refers to the second ITF-off run only. Because the ECCO LLC270 is a volume-conserving Boussinesq model, it does not reproduce the global mean sea level change. Therefore, the global mean sea level was subtracted prior to the analysis (Greatbatch, 1994).

2.2   Model for sea level variability

The westward propagation of Rossby waves and eddies provides the primary mechanism for both the ocean tunnel and the atmospheric bridge effects to transfer energy across the SIO. Under the longwave approximation, these processes can be quantified by a 1.5-layer reduced-gravity model (e.g., Qiu, 2002), which has also been widely used to investigate the variability of sea level in the SIO (e.g., Zhuang et al., 2013; Jin et al., 2018; Menezes and Vianna, 2019; Volkov et al., 2020; Nagura and McPhaden, 2021). This reduced-gravity model, hereafter called the RG model, is governed by the following linear vorticity equation, which separates the impacts of sea level signals originating at the eastern boundary and those generated by local wind forcing:

$$\frac{\partial \eta}{\partial t} = c_R \frac{\partial \eta}{\partial x} - \frac{g' \nabla \times \tau'}{\rho_0 g f} - \epsilon \eta, \tag{1}$$
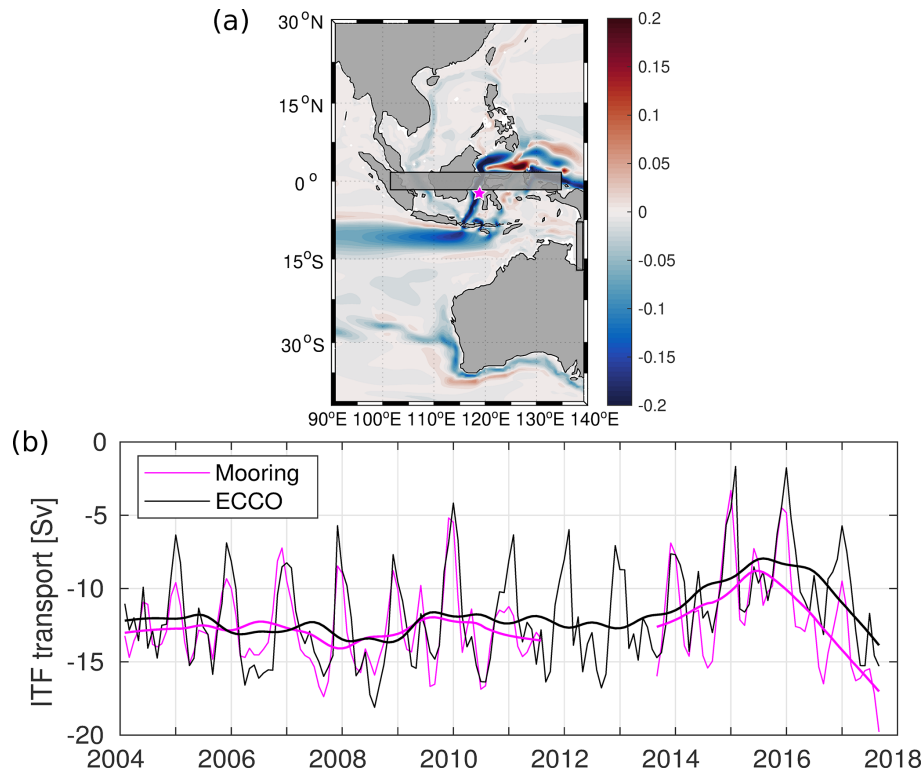
Figure 2. (a) Difference between the time-mean absolute ocean current velocities ($m\,s^{-1}$) averaged over the upper 100 m in the ITF-off and the ITF-on numerical simulations. **(b)** Monthly ITF transport in the upper 760 m from the ITF-on numerical simulation (black line) and in situ velocity measurements (magenta line) from subsurface moorings across the Makassar Strait (magenta star in **a**). The bold lines represent the low-pass-filtered time series with a cutoff period of 1 year.

where η is the baroclinic component of sea level anomaly (SLA), x is the longitude, t is the time, c_R is the zonal phase speed of long baroclinic Rossby waves, g is the gravitational constant, g' is the reduced gravity, τ' is the wind stress anomaly vector, ρ_0 is the mean sea water density, f is the Coriolis parameter, and ε is the damping coefficient.

Integrating Eq. (1) westward from the eastern boundary (x_e) along the baroclinic Rossby wave characteristics yields the following solution (Qiu, 2002):

$$\eta(x,t) = \eta\left(x_e, t - \frac{x - x_e}{c_R}\right) e^{\frac{-\epsilon}{c_R}(x - x_e)}$$
$$- \frac{g'}{\rho_0 g f c_r} \int_{x_e}^{x} \nabla \times \tau'\left(x', t - \frac{x - x'}{c_R}\right) e^{\frac{-\epsilon}{c_R}(x - x')} \mathrm{d}x'. \quad (2)$$

The first term on the right side of Eq. (2) represents the SLA signal that originates at the eastern boundary. The second term represents the SLA signal generated by the local wind stress curl. Both signals propagate westward and decay at a rate determined by the damping coefficient, ε. The RG model was initialized with the low-pass-filtered SLA at 110° E, $\eta(x_e, t)$, obtained from the two numerical simulations (ITF-on and ITF-off) at 13 and 25° S (similar to Nagura and McPhaden, 2021). The model was forced with the ECCO

LLC270 wind stress and integrated from 110 to 50° E. It should be noted that the eastern boundary at 13° S is located further east at $\sim$ 130° E. However, because $\eta(x_e, t)$ at 110 and 130° E are strongly correlated ($R = 0.80$), we initialize the model for both latitudes at 110° E for consistency. The RG model parameters were obtained empirically, and they are summarized in Table 1. Specifically, the phase speeds (c_R) were set to $6.5\,cm\,s^{-1}$ at 25° S and $13\,cm\,s^{-1}$ at 13° S, based on the Hovmöller diagrams of the altimetry and model SLA in the SIO (see Sect. 3.1). These phase speeds are consistent with those estimated by Nagura and McPhaden (2021). The optimal values of g' and ε were obtained iteratively using a linear regression. The zonal mean g' varies from $0.05\,m\,s^{-2}$ at 25° S to $0.07\,m\,s^{-2}$ at 13° S for the ITF-on experiment and from $0.04\,m\,s^{-2}$ at 25° S to $0.07\,m\,s^{-2}$ at 13° S for the ITF-off experiment, reflecting the meridional variation in stratification (Zhuang et al., 2013). A regression analysis yielded the following optimum damping coefficients: $\varepsilon^{-1} = 2.5$ years at 13° S and $\varepsilon^{-1} = 1.9$ years at 25° S for the ITF-on experiment, and $\varepsilon^{-1} = 3.3$ years at 13° S and $\varepsilon^{-1} = 1.2$ years at 25° S for the ITF-off experiment (Table 1).

Table 1. Summary of the parameters used in the RG model.

SLA forcings	Simulation	c_R (cm s^{-1})	g' (m s^{-2})	ε^{-1} (years)
SLA at 13° S and 110° E	ITF-on	13.0	0.07	2.5
	ITF-off	13.0	0.07	3.3
SLA at 25° S and 110° E	ITF-on	6.5	0.05	1.9
	ITF-off	6.5	0.04	1.2

2.3 Data

Steric or density-driven changes dominate large-scale sea level variability on seasonal-to-interannual timescales (e.g., Gill and Niller, 1973). The monthly maps of altimetry SLA from 1993 to 2019 provided by the Copernicus Marine Environment Monitoring Service (CMEMS; Ducet et al., 2000) were used to validate the sea level changes simulated by the ECCO LLC270 model. The global mean sea level rise was subtracted from SLA maps to focus on regional variations. Since density variations in low latitudes and midlatitudes are mainly caused by temperature variations, satellite measurements of sea level can be used as a proxy for OHC (Roemmich and Gilson, 2009). To illustrate this point in the SIO, we compared the OHC anomaly time series for the upper 2000 m (Levitus et al., 2012) with the altimetry SLA variability averaged over 55 to 115° E and 10 to 30° S (green and red lines in Fig. 1a, respectively). The time series are strongly correlated ($R = 0.90$), confirming that SLA is a good indicator of OHC changes in the SIO.

To link the observed variability in the ocean to ENSO, we used the MEI, provided by the National Oceanic and Atmospheric Administration (NOAA) Earth System Research Laboratory's Physical Sciences Division (http://www.esrl.noaa.gov/psd, last access: 5 February 2022), which incorporates both oceanic and atmospheric variables to provide a single index of ENSO intensity. This monthly index integrates the impact of five factors over the tropical Pacific basin (sea level pressure, sea surface temperature, zonal and meridional components of the surface wind, and outgoing longwave radiation). Positive MEI events are related to warm, El Niño conditions, and negative MEI events are related to cold, La Niña conditions (Fig. 1a). We also employed the monthly DMI provided by the NOAA Earth System Research Laboratory (Saji and Yamagata, 2003). The DMI is an indicator of the IOD, defined as the difference between averaged sea surface temperature over the western equatorial Indian Ocean (50–70° E, 10° S–10° N) and the southeastern equatorial Indian Ocean (90–110° E, 10–0° S). Finally, we used the monthly Marshall SAM index from British Antarctic Survey (Marshall, 2003; http://www.nerc-bas.ac.uk/icd/gjma/sam.html, last access: 5 February 2022), which is based on available station-based zonal pressure observations between 40 and 65° S.

2.4 Statistical analysis

To identify the dominant spatiotemporal modes of SLA variability in the Indian Ocean, an empirical orthogonal function (EOF) analysis was carried out using the MATLAB Climate Data Toolbox (Monahan et al., 2009; Greene et al., 2019). The obtained spatial patterns of the variability are referred to as EOFs, and their temporal evolutions are shown by principal component (PC) time series. Prior to computing the EOFs, the global mean sea level, the seasonal cycle, and the linear trend were subtracted from the data. Then the data were low-pass filtered with a cutoff period of 1 year to focus on the interannual-to-decadal variability. The spatial patterns of EOFs are represented as regression maps obtained by projecting SLA onto the standardized (divided by standard deviation) PC time series. Thus, the regression coefficients are in centimeters (local change of sea level) per standard deviation of change in the PC. The linear regression analysis was also performed to relate the SLA to atmospheric circulation patterns (i.e., the meridional surface wind stress). Using these regression coefficients, we reconstructed the SLA time series at each grid point associated with the PC or the meridional wind stress variability. The relative contribution of the eastern boundary and the local wind stress forcing terms is represented by the explained variance, which is calculated as the fraction of variance (F) of a variable x, explained by another variable y:

$$F = 100\% \times \left[1 - \frac{\text{var}(x - y)}{\text{var}(x)} \right].$$

3 Results

3.1 Variability of sea level in the Indian Ocean

Before exploring the ocean processes related to sea level changes in the ITF-on and ITF-off experiments, we first validate the model's performance by comparing the modeled upper-ocean ITF transport with that obtained from moored velocity measurements across the Makassar Strait, which is the primary ITF gateway (Fig. 2a; Gordon et al., 1999, 2010; Pujiana et al., 2019). The agreement between the two monthly transport time series is rather good (Fig. 2b), with a correlation of 0.81. Over the period of 2004–2017, with a gap from August 2011 to August 2013, the observed and simulated mean ITF transports are −12.5 and −11.6 Sv (minus sign indicates southward transport), respectively. The low-pass-filtered time series clearly shows a pronounced reduction of the upper-ocean ITF transport in 2014–2016 in both the ITF-on experiment and in observations. This anomalous ITF transport is primarily a response to the strongest El Niño to date in the 21st century, followed by the strongest negative IOD on record (Fig. 1a; Pujiana et al., 2019). The record maximum ITF transport in 2017 reported by Gordon et al. (2019) is also simulated well by the model. The real-

istic representation of the ITF in the ECCO LLC270 model gives confidence that closing the Indonesian passages in the ITF-off experiment will help to better explain the impact of the ITF on the variability of sea level and OHC in the SIO. The closure of the ITF leads to a weakening of the SEC and the LC, as demonstrated by the difference between the time-mean upper 100 m velocities in the ITF-off and the ITF-on experiments (Fig. 2a). This is consistent with the results of Lee et al. (2002), who also conducted a numerical experiment with closed Indonesian passages.

ENSO excites zonal wind variability in the equatorial Indian Ocean via changes in the Walker circulation (e.g., Xie et al., 2002), which generates equatorial Kelvin waves (e.g., Chambers et al., 1999; Feng and Meyers, 2003). These waves can eventually get trapped along the Indonesian coast and partly propagate southward. The coastal trapped waves intrude into the Indonesian seas through passages between the islands (Molcard et al., 1996; Durland and Qiu 2003; Syamsudin and Kaneko, 2004; Pujiana et al., 2013; Pujiana and McPhaden, 2020) and then penetrate the western Pacific (Wijffels and Meyers 2004; Yuan et al., 2018) without significantly affecting the dynamics along the Australian coast. In the ITF-off experiment, an artificial wall was placed to close the Indonesian passages and the Torres Strait. Theoretically, such a wall may permit waves that originated in the eastern equatorial Indian Ocean to follow the artificial coastline, pass through the Indonesian Archipelago, and reach the western coast of Australia. If this is the case, then closing the ITF would generate spurious variability in the ESIO.

To verify this possibility, we carried out a cross-correlation analysis of the daily low-pass-filtered (with a cutoff period of 1 year) SLA output at a number of locations along Indonesian and Australian coastlines in both the ITF-on and the ITF-off experiment (Fig. 3). Apparent signal propagation is observed between Points 1 and 4 but is not traceable in the Timor Passage (Point 5) and further east, indicating that the incoming Indian Ocean Kelvin wave energy transmits southeastward along the southern coasts of Sumatra, Java, and Nusa Tenggara, with part of the energy making its way into Makassar Strait. Most coastal trapped wave energy appears to leak and dissipate in the internal Indonesian seas. Both experiments exhibit similar cross-correlation functions with maximum values at the same time lags for Points 1–4 (Fig. 3b, c). It takes about 10 d for the signal to propagate from the Equator to Point 4 (the distance of approximately 2500 km), which yields the wave phase speed of about 3 m s^{-1}. Further east at Points 5–7, the cross-correlations do not suggest a continued wave propagation (Fig. 3b, c). The propagation of coastal trapped waves is also observed along the northwestern and western Australian coast (Fig. 3a). The lagged correlations are observed between Points 8 and 12, and the high-frequency SLA variability at these points is uncorrelated with the high-frequency SLA variability in the Torres Strait at Point 7 (Fig. 3d, e). In both experiments, it takes about 7 d for a coastal trapped wave to propagate approxi-

mately 5000 km from Point 8 to Point 12, which yields the phase speed of about 5 m s^{-1}. Overall, coastal trapped waves appear to propagate and dissipate similarly in both the ITF-on and the ITF-off experiments, meaning that the artificial wall created in the ITF-off experiment is unlikely to generate spurious variability in the ESIO.

The 2004–2013 linear trend of SLA derived from satellite altimetry (Fig. 1b) shows two well-outlined regions of positive trend values: the first region occupies most parts of the northern and equatorial Indian Ocean, while the second region is confined to the SIO extending off the western coast of Australia westward between 55 to 115° E and 10 to 30° S (Box A). The time series of altimetry SLA averaged over Box A shows a persistent increase in 2004–2013 (Fig. 4a). In 2014, sea level reached a decadal maximum, after which it decreased abruptly following the 2014–2016 El Niño. After reaching a local minimum in 2016, it partially recovered by the end of 2017. The observed SLA variability is simulated well by the ITF-on experiment (compare the red and black curves in Fig. 4a; $R = 0.80$). In contrast, there was no pronounced increase of SLA in 2004–2013 in the ITF-off experiment (dashed black curve in Fig. 4a), which suggests the dominant role of the ITF in driving this decade-long change. The ITF-off experiment also shows a decrease of SLA in 2014–2016, although the magnitude of this decrease was smaller than in the ITF-on simulation by about a factor of 2 (solid and dashed black curves in Fig. 4a; $R = 0.38$ between the two simulated SLA).

It has been shown that the relative importance of remote and local drivers for sea level variability in the SIO depends on longitude and latitude (Volkov et al., 2020; Nagura and McPhaden, 2021). Based on these findings, we examined the SLA averaged over three different areas within box A (see insert in Fig. 4). The time series of the observed and simulated SLA averaged over the WSIO at low latitudes (from 10 and 17° S; box B in Fig. 4) are closely aligned throughout the entire period ($R = 0.94$). It appears that the closure of the Indonesian passages does not significantly change the interannual variability of SLA in this area (Fig. 4b; $R = 0.82$ between the observed and simulated SLA). Decadal tendencies are also similar in the two simulations over the ESIO at low latitudes (from 10 and 17° S; box C), although the interannual variability is somewhat different (Fig. 4c; $R = 0.78$ in the ITF-on experiment and $R = 0.14$ in the ITF-off experiment). In contrast, the time series of SLA averaged over the SIO at midlatitudes (from 17 and 35° S; box D) exhibit behaviors similar to the SLA time series averaged over the entire box A: (i) there is no significant increase of SLA in 2004–2013, and (ii) the magnitude of the 2014–2016 SLA is reduced by a factor of 3 in the ITF-off simulation compared to the ITF-on simulation (Fig. 4d). The correlation coefficients between the SLA time series observed by satellite altimetry (red curves) and simulated in the ITF-on (solid black curve) and the ITF-off (dashed black curve) experiments are 0.86 and 0.45, respectively. These results suggest that the
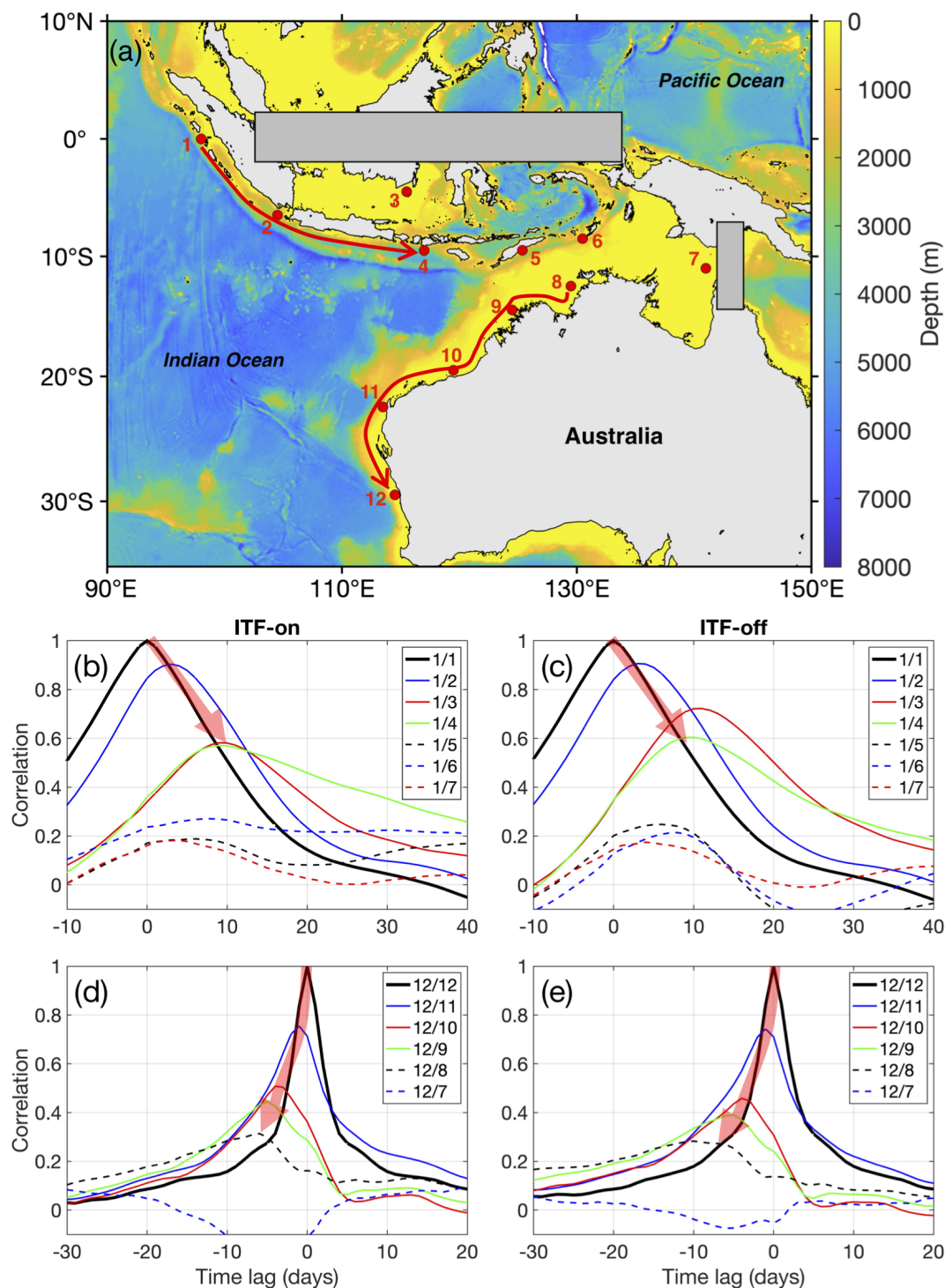
Figure 3. (a) Bottom topography in the ESIO and the locations (1 to 12) used for cross-correlation analysis. Cross-correlation functions between the daily SLA in **(b, d)** the ITF-on and **(c, e)** the ITF-off simulations. The locations 1 and 12 are used as reference points to detect waves propagating along the Maritime Continent from 1 to 7 **(b, c)** and along the west Australian coast from 7 to 12 **(d, e)**. The red arrows connect the peaks of cross-correlation functions associated with coastal trapped waves.
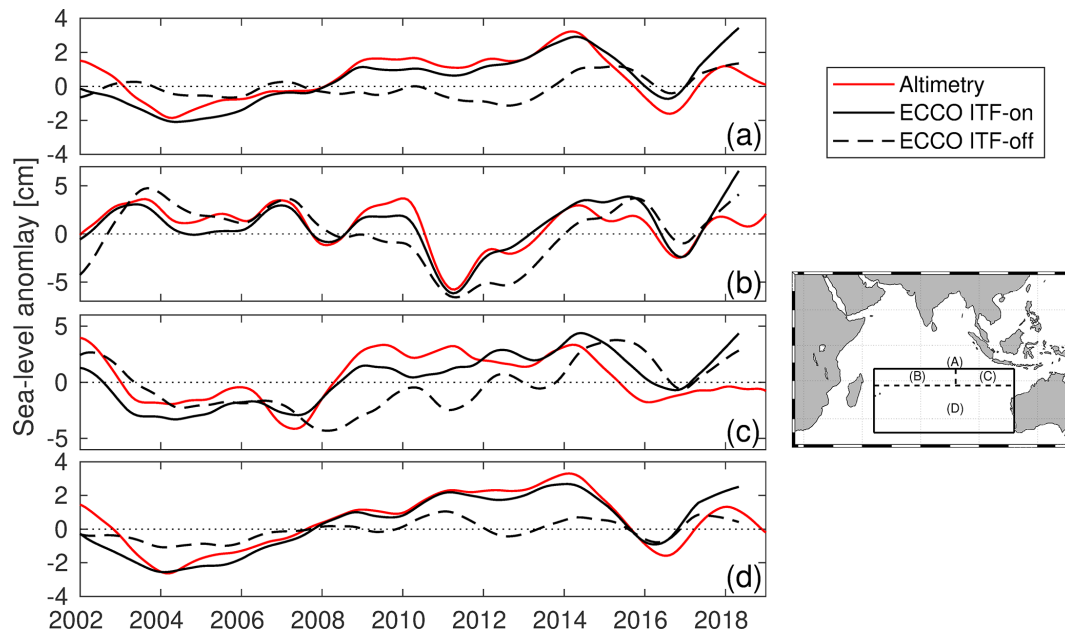
Figure 4. Time series of the sea level anomaly (SLA) from altimetry (red line) and from numerical simulations (ITF-on: black line; ITF-off: black dashed line). The SLA **(a, b, c, d)** are averaged in four areas (A, B, C, D, respectively) represented in the map on the right panel. All the time series are low-pass filtered with a cutoff period of 1 year.

decade-long increase of SLA in 2004–2013 and the development of SLA anomaly in the SIO in 2014–2016 are mostly due to remote forcing, while local forcing is more important at low latitudes.

While investigating the relative importance of each mode of atmospheric variability goes beyond the scope of this paper, it has been shown that all of these climate modes can influence the interannual-to-decadal variability of sea level in the SIO, but none of them alone is able to explain the whole complexity of the local wind forcing (Volkov et al., 2020). The squared correlation coefficients between the ENSO, IOD, and SAM indices (see Sect. 2.3) and the SLA averaged over the boxes B, C, and D quantify to what extent the variance of these three climate modes explain the variance of SLA (percent variance). ENSO explains 58 % of the SLA variance in box B with no time lag, while its influence is significant in box C with a time lag of 13 months (percent variance of 36 %). No other significant relationships were found.

The westward propagation of interannual SLA signals has been the most prevalent characteristic of the spatiotemporal SLA variability in the SIO over the entire period of both the altimetry observations and the numerical simulations, as seen in the Hovmöller diagrams of SLA (Fig. 5a–c). The altimetry data (Fig. 5a) and the ITF-on simulation (Fig. 5b) show similar signals detected at the eastern boundary reaching the western boundary 2–3 years later. For example, the two strongest positive SLA at the eastern boundary in 1999–2001 and in 2010–2013 associated with La Niña conditions

reached 50° E in 2002–2003 and in 2014, respectively. A negative SLA driven by the 1997–1998 El Niño reached 50° E in 2000. It is interesting to note that the amplitude of the 1997–1998 (1999–2001) anomaly increased (decreased) to the west of the Ninety East Ridge. It also appears that local processes can sometimes suppress and prevent signals from crossing the Ninety East Ridge. The 2003–2007 negative anomaly is an example of a negative SLA signal that did not travel far past the Ninety East Ridge. The signals simulated in the ITF-off experiment (Fig. 5c), including those emanated from the eastern boundary (Fig. 5d), generally have smaller amplitudes than those observed in the ITF-on simulation and in observations, but the spatial and temporal structures of the signals are similar. This indicates that local processes and wind forcing in the SIO, possibly related to the atmospheric bridge effect, are important drivers for the regional sea level and OHC changes.

The large-scale spatiotemporal changes of SLA were also studied with an EOF analysis. In the ITF-on simulation, the leading EOF (EOF1; Fig. 6a) explains 44 % of the interannual SLA variance, and it reveals a dipole structure with a positive anomaly over the central and western tropical Indian Ocean and a negative anomaly along the eastern boundary and around the Maritime Continent (Fig. 6a). The regression of wind stress on the PC1 (Fig. 6a) shows that the first EOF is linked to ENSO associated with weaker trade winds in the SIO and easterly wind anomalies along the Equator. This atmospheric circulation pattern favors upper-ocean warming in the northwestern SIO and cooling in the southeast-
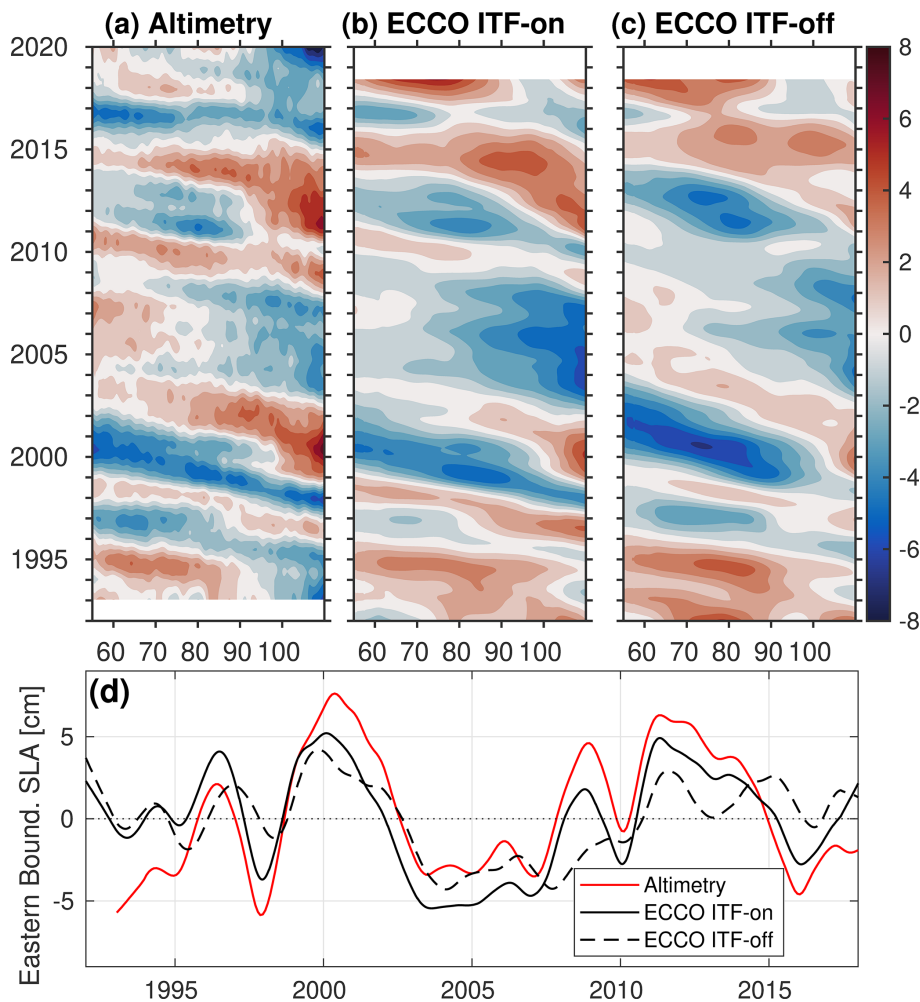
Figure 5. Hovmöller diagrams of **(a)** the observed SLA, **(b)** the ECCO-modeled SLA from the ITF-on simulation, and **(c)** the ECCO-modeled SLA from the ITF-off simulation, averaged between 10 and 30° S. **(d)** Time series of SLA from altimetry (red line) and from numerical simulations (ITF-on: solid black line; ITF-off: dashed black line), averaged between 10 and 30° S at 110° E. All of the time series are detrended and low-pass filtered (with a cutoff period of 1 year).

ern SIO, leading to positive and negative SLA, respectively. The EOF1 in the ITF-off simulation explains 41.1 % of the variance (Fig. 6b), and it displays very similar large-scale features. However, one can notice that the positive loading of the dipole in the central Indian Ocean is intensified and extends further east and that the area of cold anomaly adjacent to the western Australian coast becomes narrower. It can probably be explained by the weaker SEC and LC in the ITF-off experiment (Fig. 2a). This comparison suggests that the spatial variability pattern is mostly determined by local processes not related to the ocean tunnel effect.

The PC1 time series of both the ITF-on and the ITF-off simulations are highly correlated ($R = 0.97$; Fig. 6c, d). There are two distinct peaks in 1997–1998 and in 2014–2016 that coincided with the two strongest El Niño events on record (Fig. 1a). We reconstructed SLA using only the EOF1 for both the ITF-on and the ITF-off experiments. The local

SLA variance explained by the EOF1 is shown in Fig. 6 (e and f). One can see that the reconstruction explains greater than 70 % of the SLA variance over the central and western tropical Indian Ocean and along the eastern boundary in both experiments. While the experiments display very similar large-scale patterns, the EOF1 for the ITF-on simulation is responsible for somewhat greater variance explained along the eastern boundary.

Along with the signals coming from the equatorial Pacific, the variability of sea level and OHC along the western Australian coast is also driven by alongshore winds. These winds are modulated by ENSO via the atmospheric bridge effect. As follows from the regression of wind and Ekman pumping anomalies on MEI (Fig. 7a), El Niño events (i.e., positive MEI) are associated with weaker trade winds in the SIO and easterly wind anomalies along the Equator. This atmospheric circulation pattern favors a negative (into the ocean) Ekman
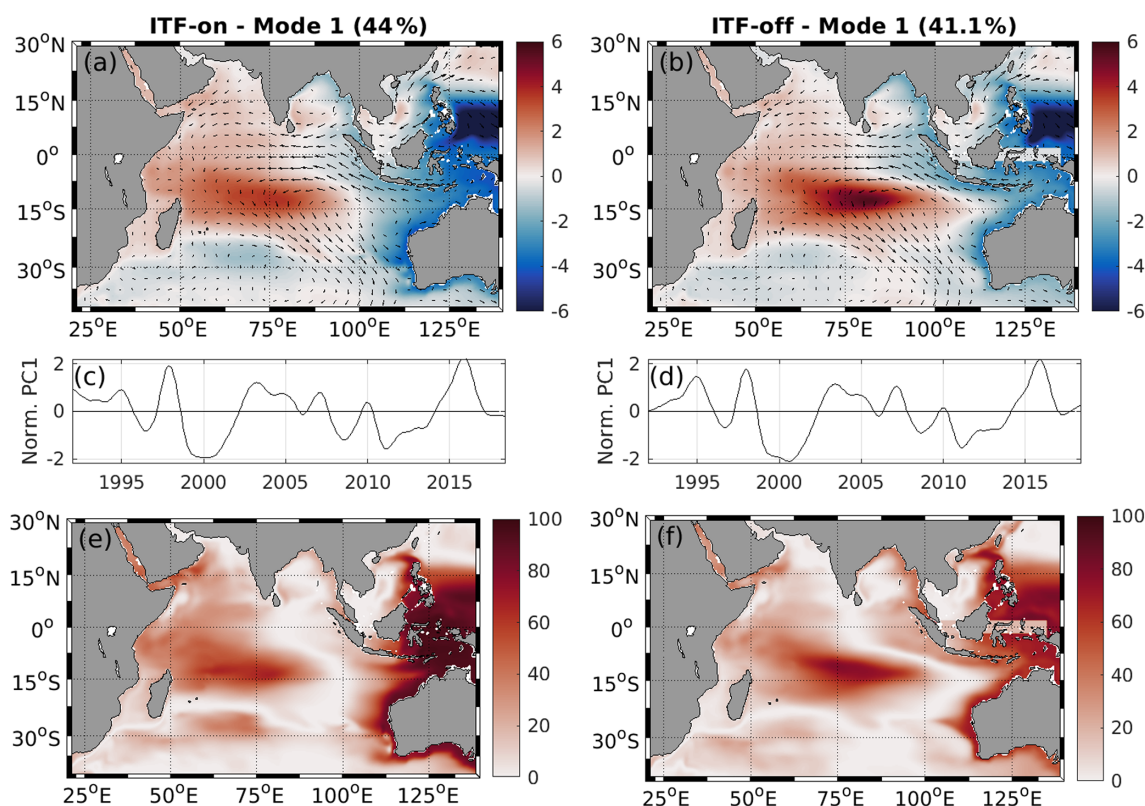
Figure 6. Regression of monthly SLA (color) and wind stress (arrow) on the standardized principal component of the first EOF mode (PC1) from 1992 to 2018 for the ITF-on **(a)** and ITF-off **(b)** simulations, expressed in centimeters per 1 SD of change of the respective PC1. **(c, d)** Time evolution of the associated PC1 normalized by their standard deviations. **(e, f)** Explained variance between the modeled and the reconstructed SLA.

pumping anomaly along the western Australian coast, resulting in upper-ocean warming. The opposite occurs during La Niña events (i.e., negative MEI). The regression of the monthly modeled SLA on the monthly wind stress averaged over 110–115° E and 20–35° S (rectangles in Fig. 7b, c) is presented for both the ITF-on (Fig. 7b, d) and the ITF-off (Fig. 7c, e) simulations. The regression shows that northward and southward wind anomalies along the western Australian coast favor lower and higher sea level along the coast, respectively, with a lower amplitude in the ITF-off experiment compared to the ITF-on simulation. As expected, the results suggest the importance of upwelling and downwelling off the coast favored by southerly and northerly wind anomalies, respectively. Note that the area close to the western Australian coast is characterized by the strongest positive meridional wind stress in the Indian Ocean and elevated standard deviations (not shown). The reconstruction of SLA using the obtained regression coefficients demonstrates that the alongshore winds over the 1992–2018 time period explain 15 % and 11 % of the SLA variance in the ESIO in the ITF-on and ITF-off simulations, respectively. It should be noted that this relationship is time dependent and becomes significant if we focus on the 2004–2018 time period. Over this time period,

the alongshore winds explain 25 % and 36 % of the SLA variance in the ESIO in the ITF-on and ITF-off simulations, respectively. The remaining variability can be explained by instabilities of the LC generating mesoscale eddies in the area and coastal trapped waves originating along the northwestern coast of Australia (e.g., Zheng et al., 2018).

3.2 Local vs. remote forcing mechanisms

Here we quantify and assess the combined and relative contributions of the eastern boundary forcing and the local wind stress curl to the interannual variability of SLA in the SIO using the 1.5-layer RG model (see Sect. 2.2) at 13 and 25° S for both the ITF-on and the ITF-off simulations.

In the ITF-on experiment, the RG model reproduces the SLA variability reasonably well (Figs. 8 and 9, green curves). The fractions of SLA variance in the ECCO model explained by SLA reproduced by the RG model at 13° S (at 25° S) are equal to 69 % (64 %) in the WSIO and 88 % (82 %) in the ESIO. The relative contributions of the eastern boundary and the local wind stress forcing terms are estimated by computing the fraction of SLA variance in the total RG model (the sum of the eastern boundary and local wind forcing) explained by the individual forcing components. In the RG
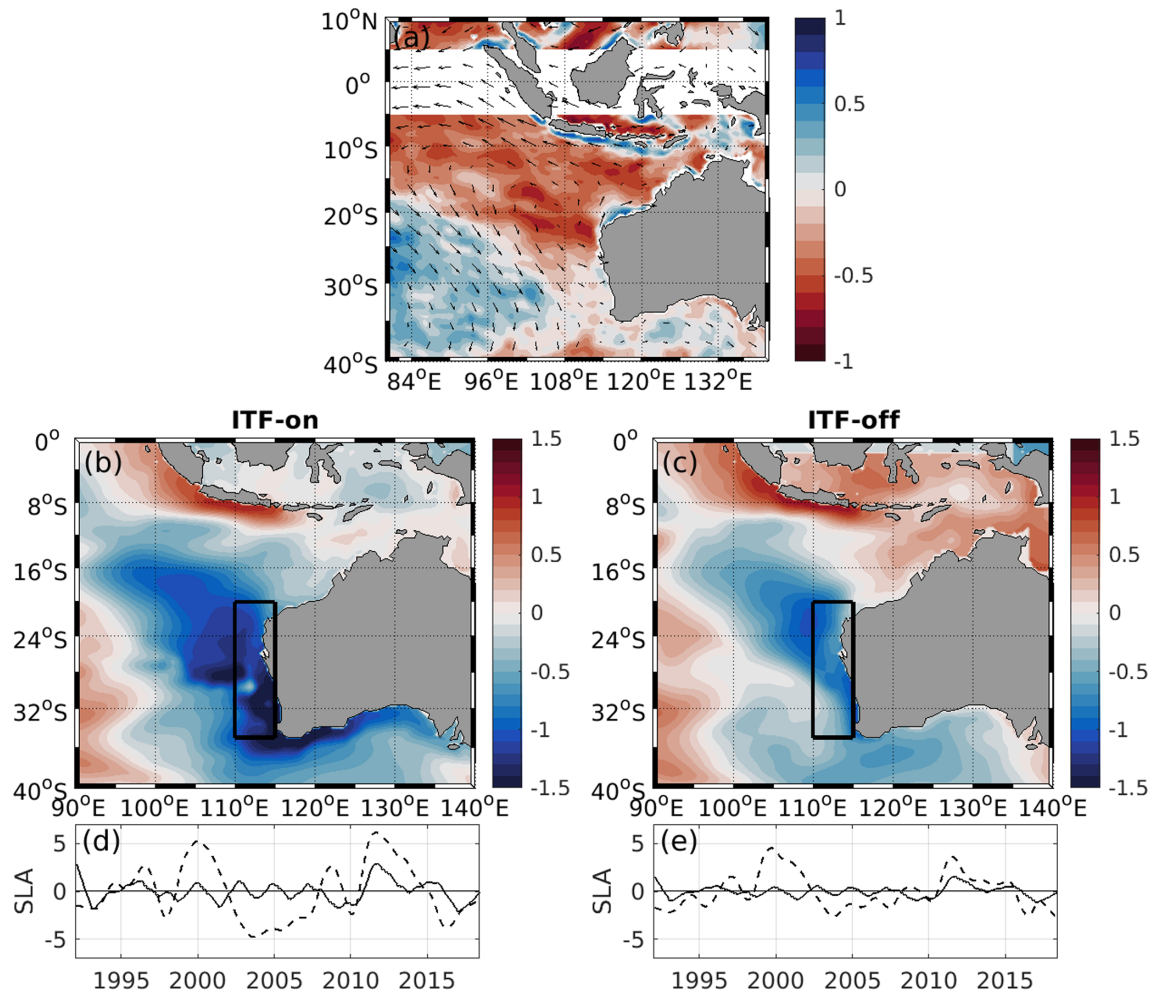
Figure 7. (a) Regression of Ekman pumping (color shading) and wind stress (arrows) on MEI, expressed in meters per month per standard deviation of change in the index. Negative (positive) Ekman pumping anomalies associated with the upper-ocean warming (cooling) are shown by red (blue) color. Regression of monthly SLA on the normalized meridional surface wind stress from 1995 to 2018 averaged in the black box for the ITF-on **(b)** and ITF-off **(c)** simulations, expressed in centimeter per 1 SD of change of the meridional surface wind stress $(1\,\mathrm{SD} = 0.045\,\mathrm{N\,m^{-2}})$. **(d, e)** Time evolution of the reconstructed SLA (solid black line) and modeled SLA (dashed black line) associated with the regression from the ITF-on and ITF-off simulations.

model, the simulated SLA variability in the ESIO is dominated by the eastern boundary forcing (Figs. 8c, g and 9b, d), which explains 62 % (90 %) of the SLA variance at 13° S (25° S). The local wind forcing becomes the main driver of the SLA variability in the WSIO at 13° S, explaining 70 % of the SLA variance (Figs. 8b, d and 9a). At 25° S, none of the forcing components explains any variance in the WSIO. Nevertheless, the amplitudes of the two forcing components are similar, meaning that their contribution to the SLA variability is comparable (Figs. 8g, h and 9c). Overall, the local wind stress curl over the WSIO is able to either strongly modify the SLA originating from the eastern boundary or generate new anomalies that also propagate westward.

We also applied the 1.5-layer RG model at 13 and 25° S for the ITF-off simulation (Fig. 10). Once again, the RG model

is able to reasonably reproduce the ECCO LLC270 SLA, in particular at 13° S (Figs. 10a, b and 11, green curves). The RG model explains 69 % (13 %) of the ECCO-modeled SLA variance at 13 ° S (at 25 ° S) in the WSIO and 81 % (31 %) in the ESIO. The signals simulated in the ITF-off experiment (Fig. 10) generally have the same characteristics as those simulated in the ITF-on experiment but with somewhat smaller amplitudes at 25° S (Fig. 8). The local wind forcing appears to be the main driver for SLA variability at 13° S in the WSIO, explaining 78 % of the SLA variance in the RG model (Figs. 10b, d and 11a). Similar to the ITF-on experiment, neither of the forcing components explains any SLA variance at 25° S in the WSIO, but their amplitudes are similar. The eastern boundary forcing dominates at both lati-
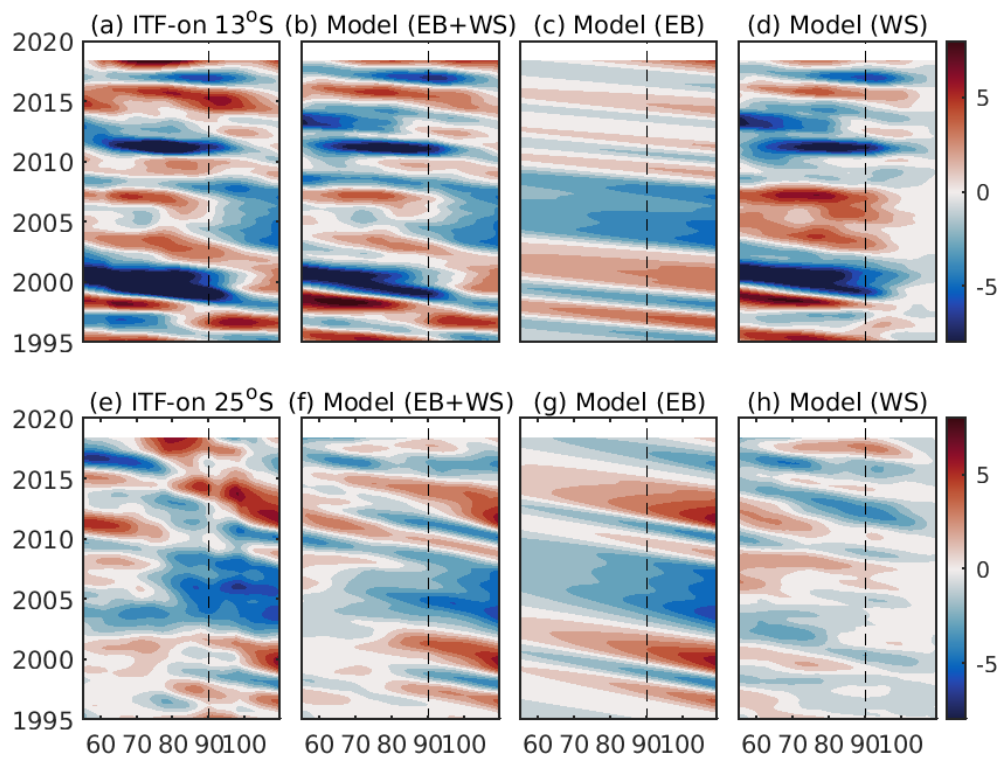
Figure 8. Hovmöller diagrams of **(a, e)** the ECCO-modeled SLA at 13 and 25° S from the ITF-on simulation, **(b, f)** the RG-modeled SLA using both the eastern boundary and the local wind stress curl forcing, **(c, g)** the RG-modeled SLA obtained using the eastern boundary forcing only, and **(d, h)** the RG-modeled SLA obtained using the local wind stress curl forcing only. The results from the ITF-on simulation at 13° S are shown in the top panels, and those at 25° S are shown in the bottom panels.
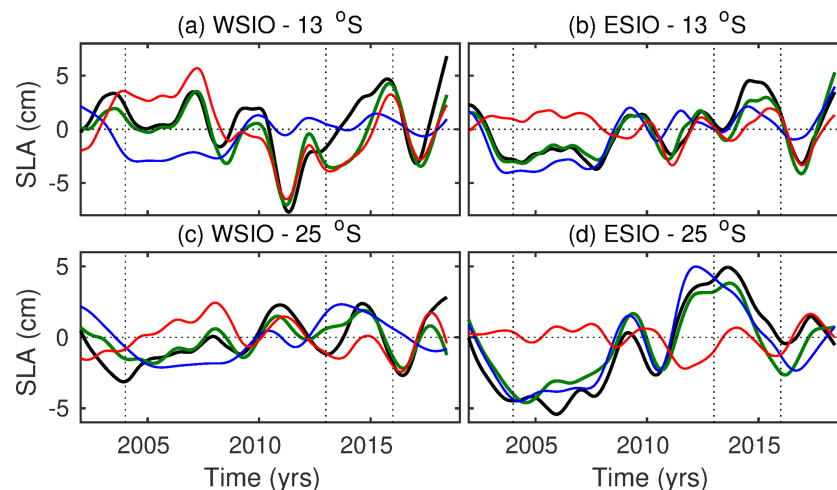
Figure 9. Time series of the simulated ECCO LLC270 SLA from the ITF-on simulation (black curves) and RG-modeled SLA using the eastern boundary forcing (blue curves), the local wind stress curl forcing (red curves), and both forcing terms (green curves), averaged between **(a, c)** 55–90° E and **(b, d)** 90–110° E at 13° S **(a, b)** and 25° S **(c, d)**. Vertical dashed lines indicate the years 2004, 2013, and 2016.

tudes in the ESIO in the ITF-off experiment, explaining 70 % (90 %) of the SLA variance at 13° S (25° S) (Fig. 10f, g).

3.3 Meridional transport of the subtropical gyre

The large-scale sea level variability in the subtropical SIO reflects the meridional transports associated with the meridional overturning circulation (MOC) in the Indian Ocean (Zhuang et al., 2013; Nagura, 2020). Due to the connection between the Pacific Ocean and Indian Ocean via the Indonesian passages, these transports play a fundamental role in the inter-ocean exchange of mass, heat, salt, and carbon within the global climate system. A diagnosis of the Indian Ocean meridional transports is thus important for our understanding of the global climate and its variability (e.g., Wang, 2019). The zonal gradient of SLA between the western and eastern regions of the subtropical SIO can be used as a proxy for this zonally integrated meridional transport (Zhuang et al., 2013; Nagura, 2020). Displayed in Fig. 12 (c, d) are the zonal differences between SLA averaged over 50–55° E (SLA_{west}) and 110–115° E (SLA_{east}) as a function of latitude (15–30° S) and time in both the ITF-on and the ITF-off simulations. The differences between these two simulations are used to diagnose the relative importance of the ocean tunnel and atmospheric bridge effects on the interannual variability of the meridional transport.

In the ITF-on simulation (Fig. 12c), the zonal (west–east) differences of SLA are clearly related to ENSO (see MEI in Fig. 12a, b): the positive differences (in 1997–1998, 2002–2007, 2009–2010, and 2014–2016) are generally associated with El Niño conditions (cold anomalies in the ESIO) and the negative differences (in 1999–2001, 2008, 2011–2013) are associated with La Niña conditions (warm anomalies in the ESIO). The correlation between the MEI and the west–east SLA differences in the ITF-on experiment across the latitudinal band considered (15–30° S) ranges between 0.51–0.81, with a maximum correlation at 27° S (not shown). In the ITF-off experiment, the correlation between the MEI and the west–east SLA differences reduces to 0–0.59, with a maximum correlation at 29° S. Nevertheless, in both the ITF-on and the ITF-off experiments, the SLA gradients exhibit similar amplitudes and patterns. For example, the persistent negative SLA gradients in 1999–2002 and the persistent positive SLA gradients in 2002–2007 are observed in both experiments. However, the shorter-term positive SLA gradients associated with the 1997–1998 and 2014–2016 El Niño events have significantly smaller amplitudes in the ITF-off experiment compared to the ITF-on experiment.

To verify the relationship between the zonal gradient of SLA and the meridional transport in the SIO subtropical gyre, we computed the zonally integrated transports across 15° S in both the ITF-on and the ITF-off simulations. This latitude is a key position where the meridional transports are used to measure the subtropical cell variability (Zhuang et al., 2013; Nagura, 2020). The transports are integrated from coast to coast and thus include contributions from the interior and boundary currents. The transport time series (not shown) at 15° S in both simulations are modestly correlated with the zonal gradients of modeled SLA at 15° S ($R = 0.49$ in the ITF-on experiment, and $R = 0.25$ in the ITF-off experiment). The maximum agreement between the transport time series at 15° S and the zonal gradients of modeled SLA is observed at 25° S, with a correlation of 0.76 in the ITF-on experiment and 0.68 in the ITF-off experiment.

The resulting time-mean stream function of the meridional flows is illustrated by the mean profiles of cumulative transport as a function of depth (Fig. 12e,f; black lines). The Indian Ocean is essentially closed in the north aside from the ITF contribution. As a result, mass conservation requires that the transport integrated over the full depth of the ocean across 15° S is equal to the ITF transport plus the freshwater balance (precipitation minus evaporation plus river runoff) in the ITF-on simulation and to the freshwater balance in the ITF-off simulation. The vertically integrated meridional flow yields a time-mean southward transport of 12.7 Sv in the ITF-on simulation and 0.17 Sv in the ITF-off simulation. The time-mean cumulative transport in the ITF-on simulation is consistent with the simulated mean ITF transports of −11.6 Sv through the Makassar Strait, which is the primary ITF gateway (Fig. 2b). In the ITF-off simulation, the mean southward flow across 15° S is compensated by the freshwater balance to the north of this latitude (net evaporation of 0.08 Sv estimated between 8–20° S in the Indian Basin; e.g., Talley, 2008).

We also computed the composites of the obtained stream functions associated with the cold anomalies (positive MEI indicating El Niño, shown as blue lines) and warm anomalies (negative MEI indicating La Niña, shown as red lines) in the ESIO in the two experiments (Fig. 12e, f). These cold and warm anomalies in the ESIO favor northward and southward transport anomalies, respectively, which is consistent with the results of both experiments. The transport increased and reduced, respectively, by 1 Sv from 100 m to the bottom in the ITF-on experiment. In the ITF-off experiment, the transport anomaly is observed mainly between 500 and 3000 m, with a maximal value of 0.7 Sv. The consistency between the stream functions demonstrates that the meridional geostrophic transport is modulated by ENSO via the atmospheric bridge effect.

4 Discussion and concluding remarks

In this study, we revisited the interplay between the remote and local drivers for the OHC and sea level variability in the SIO using an eddy-permitting ECCO LLC270 solution. The data–model comparisons demonstrated that the model performs reasonably well in simulating the circulation of the Indian Ocean, including the ITF transport. In order to better quantify the relative contribution of the remote vs. local
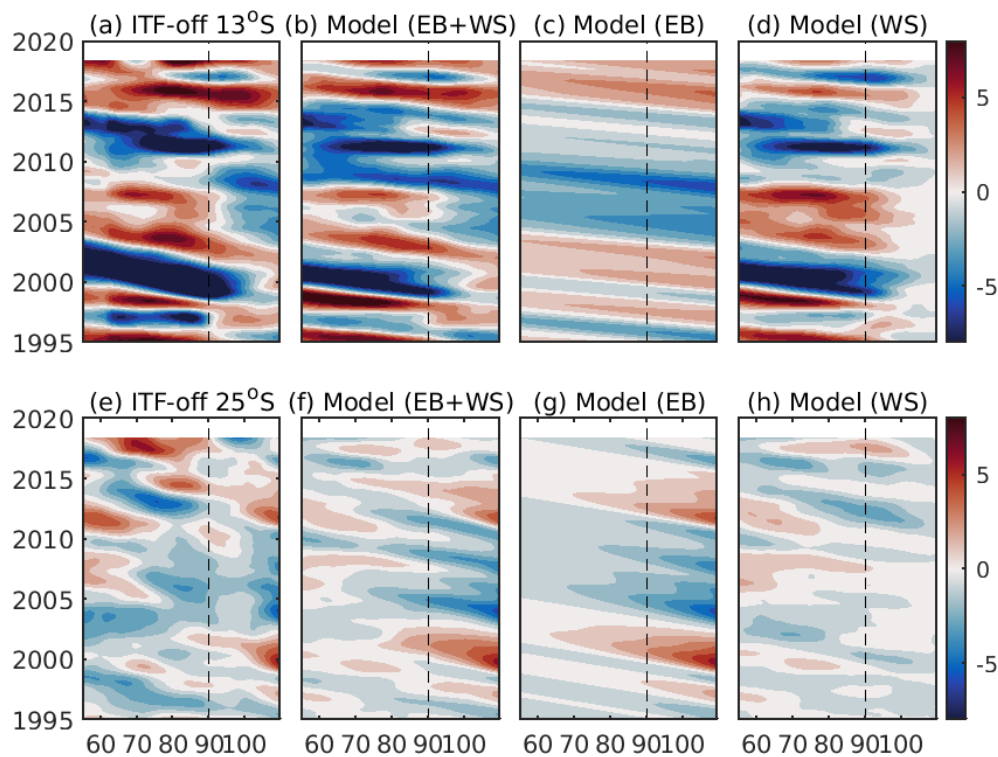
Figure 10. Hovmöller diagrams of **(a, e)** the ECCO-modeled SLA at 13 and 25° S from the ITF-off simulation, **(b, f)** the RG-modeled SLA using both the eastern boundary and the local wind stress curl forcing, **(c, g)** the RG-modeled SLA obtained using the eastern boundary forcing only, and **(d, h)** the RG-modeled SLA obtained using the local wind stress curl forcing only. The results from the ITF-off simulation at 13° S are shown in the top panels, and those at 25° S are shown in the bottom panels.
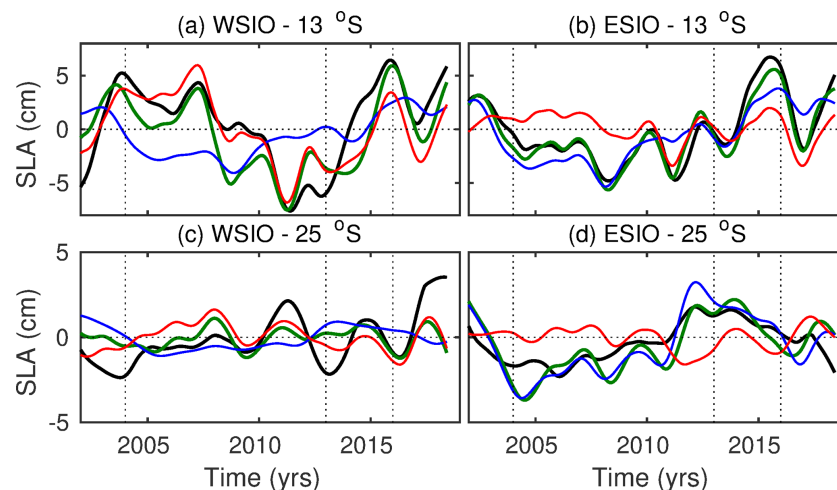
Figure 11. Time series of the simulated ECCO LLC270 SLA from the ITF-off simulation (black curves) and RG-modeled SLA using the eastern boundary forcing (blue curves), the local wind stress curl forcing (red curves), and both forcing terms (green curves), averaged between **(a, c)** 55–90° E and **(b, d)** 90–110° E at 13° S **(a, b)** and 25° S **(c, d)**. Vertical dashed lines indicate the years 2004, 2013, and 2016.
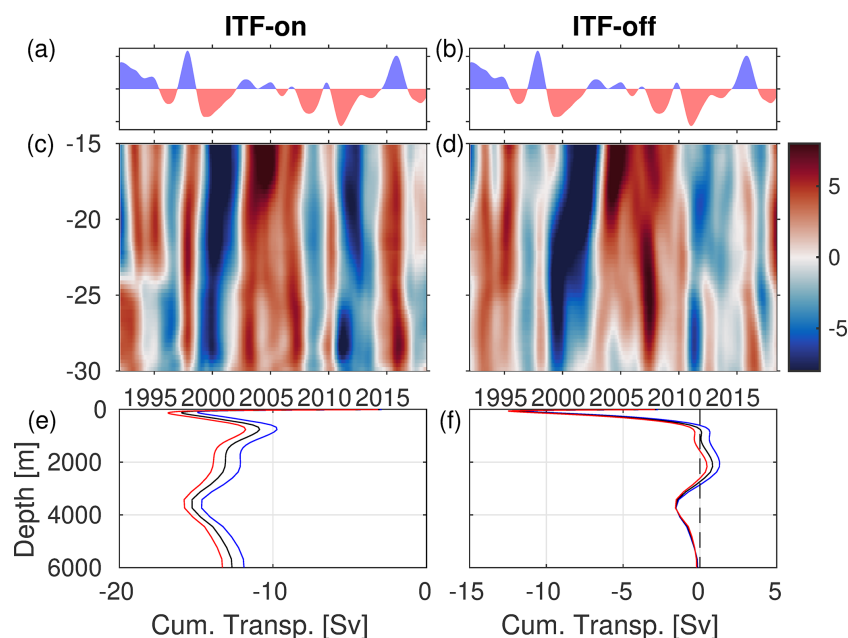
Figure 12. (a, b) Time series of the standardized MEI (El Niño and La Niña are shown by blue and red shading, respectively). **(c, d)** Zonal differences of SLA (cm) computed between 50–55° E and 110–115° E (SLA$_\text{west}$−SLA$_\text{east}$) as a function of latitude and time in the ITF-on and ITF-off experiments. **(e, f)** Time-mean stream function of the meridional flows across 15° S (black line) and the composite of the stream function associated with El Niño (blue line) and La Niña (red line) in the ITF-on and ITF-off experiments.

drivers, we conducted a sensitivity experiment with artificially closed Indonesian and Torres straits to physically separate the Indian Ocean and Pacific Ocean and eliminate the ocean tunnel effect on sea level variability in the SIO (ITF-off experiment).

The observed SLA variability in the SIO is well simulated by the ITF-on experiment showing a persistent increase from 2004 to 2014, while no pronounced increase of SLA is observed in the ITF-off experiment (Fig. 4a). This result suggests that the observed decade-long heat accumulation is due to the ocean tunnel effect, linked to the ENSO variability. Shutting the ITF off removes heat supply from the Pacific, slows down the SEC, and raises the thermocline in the SIO (Lee et al., 2002). The fact that the observed heat accumulation affected nearly the entire SIO is somewhat inconsistent with numerical tracer experiments showing that the ITF waters entering the Indian Ocean are carried mainly by the SEC (e.g., Song et al., 2004). Nevertheless, Valsala and Ikeda (2007) showed that the ITF waters can also flow along the western coast of Australia via the LC and then spread westward across the SIO.

As evidenced by satellite altimetry and Argo measurements, the decade-long accumulation of heat content in the SIO subtropical gyre ended with a strong cooling in 2014–2016. An abrupt decrease of SLA from 2014 to 2016 was simulated well in the ITF-on simulation, with an amplitude similar to satellite observations. This time period was marked by a strong El Niño, the associated reduction of southeast-

erly trade winds, and a cyclonic wind anomaly across the SIO (Volkov et al., 2020). This resulted in Ekman divergence favoring the observed upper-ocean heat content decrease. In addition, the 2014–2016 El Niño was in phase with a weak positive IOD in 2015 and the lowest negative IOD on record in 2016. These phenomena, along with a deepening of the thermocline and increased sea levels along the Maritime Continent, resulted in the reduction of the ITF transport and upper-ocean heat content (Figs. 1a, 2b). In 2014–2016, the ITF-off experiment also revealed a decrease in SLA, although the magnitude of this decline was 2 times lower than in the ITF-on simulation. This sensitivity experiment confirms that neither the atmospheric bridge nor the ocean tunnel effect alone can fully explain the observed basin-wide cooling.

The EOF analysis revealed that the spatiotemporal structures of the SLA variability in the ITF-on and ITF-off experiments are similar. The difference between the two simulations is mainly limited to the magnitude of the signals. This suggests that the spatiotemporal structure of the regional SLA and OHC variability is determined by local processes and wind forcing and is not related to the ocean tunnel effect.

Winds along the western Australian coast are part of the large-scale atmospheric circulation over the SIO dominated by southeasterly trades and modulated by ENSO via the atmospheric bridge effect. We find that these winds are able to explain only 15 % and 11 % of the SLA variability averaged

over 110–115° E and 20–35° S in 1995–2018 in the ITF-on and ITF-off simulations, respectively. The rather small impact of the alongshore wind stress on the regional SLA variability is in agreement with the study of Nagura and McPhaden (2021), who showed that the lead–lag correlation between SLA and wind forcing does not exceed the 95 % confidence level at any lag within a ±12-month window. This relationship became stronger in 2004–2018, when the alongshore winds explained greater SLA variance in the ESIO in the ITF-off simulation compared to the ITF-on simulation. This result shows the importance of the alongshore wind forcing that also drives sea level variability along the coast via the atmospheric bridge effect.

The processes driving the interannual variability of sea level and OHC in the SIO were further analyzed in the context of westward-propagating Rossby waves. Confirming previous observation-based studies (Volkov et al., 2020; Nagura and McPhaden, 2021), we showed that the relative importance of signals propagating from the eastern boundary and the local wind forcing varies with latitude (low latitude vs. midlatitude) and longitude (WSIO vs. ESIO). The time series of the simulated SLA averaged over the WSIO at low latitudes (13° S) are closely aligned in both numerical experiments. It appears that the closure of the Indonesian passages does not significantly change the interannual variability of SLA in this area. Our analysis further supports the idea that the local wind forcing appears to be the main driver for SLA variability in the tropical WSIO. Decadal tendencies are also similar in the two simulations over the ESIO at low latitudes, although the interannual variability is somewhat different. Overall, the results showed that SLA variability in the ESIO is dominated by signals radiated from the eastern boundary. At low latitudes, the interannual sea level variability is driven by the local wind forcing in the WSIO and by the eastern boundary forcing in the ESIO. This highlights the longitudinal dependence causing interannual SLA variability in the southern Indian Ocean demonstrated by Volkov et al. (2020). The variability of SLA is quite different in the two simulations at midlatitudes, although the westward propagation can be easily traced in many cases. Our results showed that the interannual variability of SLA at midlatitudes is mainly driven by waves radiated from the eastern boundary related to the ocean tunnel effect, i.e., the ITF and coastally trapped waves that rapidly transfer anomalies generated in the Pacific along the western Australian coast. This highlights the latitudinal dependence demonstrated in earlier studies (Masumoto and Meyers, 1998; Zhuang et al., 2013; Menezes and Vianna, 2019; Nagura and McPhaden, 2021).

Considering the role of the meridional overturning circulation in the mass and heat transport, it is important to examine the year-to-year variability in this circulation. We confirmed in our study that the interannual variability of the meridional transport is related to the zonal gradient of SLA between the western and eastern regions of the subtropical SIO. In both numerical simulations, the zonal SLA gradients are related to ENSO characterized by positive SLA gradients during El Niño and negative gradients during La Niña conditions. In the ITF-off experiment, the positive SLA gradients associated with the 1997–1998 and 2014–2016 El Niño events are reduced compared to the ITF-on simulation, but generally the SLA gradients exhibit similar amplitudes and patterns. Nagura and McPhaden (2021) showed that the meridional transport of the subtropical gyre is primarily driven by variability radiated from the eastern boundary. Our analysis shows that local wind forcing modulated by the atmospheric bridge effect is also an important driver for the meridional transport in the SIO subtropical gyre.

Overall, these findings advance our understanding of the regional heat content and sea level variability. To study the far-reaching impacts of the heat accumulation in the SIO, more research employing ongoing observations and ocean and climate models is necessary.

References

Allan, R., Chambers, D., Drosdowsky, W., Hendon, H., Latif, M., Nicholls, N., Smith, I., Stone, R., and Tourre, Y.: Is there an Indian Ocean dipole, and is it independent of El Niño-Southern Oscillation, CLIVAR Exchanges, 6, 18–22, 2001.

Ashok, K., Guan, Z., and Yamagata, T.: A look at the relationship between the ENSO and the Indian Ocean dipole, J. Meteorol. Soc. Jpn., 81, 41–56, 2003.

Birol, F. and Morrow, R.: Sources of the baroclinic waves in the southeast Indian Ocean, J. Geophys. Res., 106, 9145–9160, 2001.

Cai, W., Meyers, G., and Shi, G.: Transmission of ENSO signal to the Indian Ocean, Geophys. Res. Lett., 32, L05616, https://doi.org/10.1029/2004GL021736 2005.

Chambers, D. P., Tapley, B. D., and Stewart, R. H.: Anomalous warming in the Indian Ocean coincident with El Niño, J. Geophys. Res., 104, 3035–3047, 1999.

Church, J. A. and White, N. J.: Sea-level rise from the late 19th to the early 21st century, Surv. Geophys., 32, 585–602, 2011.

Clarke, A. J.: On the reflection and transmission of low-frequency energy at the irregular western Pacific Ocean boundary, J. Geophys. Res., 96, 3289–3305, 1991.

Clarke, A. J. and Liu, X.: Interannual sea level in the northern and eastern Indian Ocean, J. Phys. Oceanogr., 24, 1224–1235, 1994.

Cleverly, J., Eamus, D., Luo, Q., Restrepo Coupe, N., Kljun, N., Ma, X., Ewenz, C., Li, L., Yu, Q., and Huete, A.: The importance of interacting climate modes on Australia's contribution to global carbon cycle extremes, Sci. Rep., 6, 23113, https://doi.org/10.1038/srep23113 2016.

Dee, D. P., Uppala, S. M., Simmons, A. J., Berrisford, P., Poli, P., Kobayashi, S., Andrae, U., Balmaseda, M. A., Balsamo, G., Bauer, P., Bechtold, P., Beljaars, A. C. M., van de Berg, L., Bidlot, J., Bormann, N., Delsol, C., Dragani, R., Fuentes, M., Geer,

A. J., Haimberger, L., Healy, S. B., Hersbach, H., Hólm, E. V., Isaksen, L., Kållberg, P., Köhler, M., Matricardi, M., McNally, A. P., Monge-Sanz, B. M., Morcrette, J.-J., Park, B.-K., Peubey, C., de Rosnay, P., Tavolato, C., Thépaut, J.-N., and Vitart, F: The ERA-Interim reanalysis: Configuration and performance of the data assimilation system, Q. J. Roy. Meteor. Soc., 137, 553–597, 2011.

Domingues, C. M., Maltrud, M. E., Wijffels, S. E., Church, J. A., and Tomczak, M.: Simulated Lagrangian pathways between the Leeuwin Current System and the upper-ocean circulation of the southeast Indian Ocean, Deep-Sea Res. Pt. II, 54, 797–817, 2007.

Drushka, K., Sprintall, J., Gille, S. T., and Brodjonegoro, I.: Vertical structure of Kelvin waves in the Indonesian throughflow exit passages, J. Phys. Oceanogr., 40, 1965–1987, 2010.

Ducet, N., Le Traon, P. Y., and Reverdin, G.: Global high-resolution mapping of ocean circulation from TOPEX/Poseidon and ERS-1 and -2, J. Geophys. Res., 105, 19477–19498, https://doi.org/10.1029/2000JC900063, 2000 (data available at: https://doi.org/10.48670/moi-00148).

Durland, T. S. and Qiu, B.: Transmission of subinertial Kelvin waves through a strait, J. Phys. Oceanogr., 33, 1337–1350, 2003.

England, M. H. and Huang, F.: On the interannual variability of the Indonesian Throughflow and its linkage with ENSO, J. Climate, 18, 1435–1444, 2005.

Feng, M. and Meyers, G.: Interannual variability in the tropical Indian Ocean: a two-year time-scale of Indian Ocean Dipole, Deep-Sea Res. Pt. II, 50, 2263–2284, 2003.

Forget, G., Campin, J.-M., Heimbach, P., Hill, C. N., Ponte, R. M., and Wunsch, C.: ECCO version 4: an integrated framework for non-linear inverse modeling and global ocean state estimation, Geosci. Model Dev., 8, 3071–3104, https://doi.org/10.5194/gmd-8-3071-2015, 2015.

Fukumori, I., Wang, O., Fenty, I., Forget, G., Heimbach, P., and Ponte, R. M.: ECCO Version 4 Release 3, https://doi.org/1721.1/110380, 2017.

Gao, M., Ding, Y., Song, S., Lu, X., Chen, X., and McElroy, M. B.: Secular decrease of wind power potential in India associated with warming in the Indian Ocean, Sci. Adv., 4, eaat5256, https://doi.org/10.1126/sciadv.aat5256, 2018.

Gent P. R. and McWilliams, J. C: Isopycnal mixing in ocean circulation models, J. Phys. Oceanogr., 20, 150–155, 1990.

Gill, A. E. and Niller, P. P.: The theory of the seasonal variability in the ocean, Deep-Sea Res. Oceanogr. Abstr., 20, 2, https://doi.org/10.1016/0011-7471(73)90049-1 1973.

Gordon, A. L.: Inter-Ocean Exchange of Thermocline Water, J. Geophys. Res., 91, 5037–5046, 1986.

Gordon, A. L., Susanto, R. D., and Ffield, A.: Throughflow within Makassar Strait, Geophys. Res. Lett., 26, 3325–3328, 1999.

Gordon, A. L., Sprintall, J., Van Aken, H. M., Susanto, D., Wijffels, S., Molcard, R., Ffield, A., Pranowo, W., and Wirasantosa, S.: The Indonesian throughflow during 2004–2006 as observed by the INSTANT program, Dynam. Atmos. Oceans, 50, 115–128, 2010.

Gordon, A. L., Napitu, A., Huber, B. A., Gruenburg, L. K., Pujiana, K., Agustiadi, T., Kuswardani, A., Mbay, N., and Setiawan, A.: Makassar strait throughflow seasonal and interannual variability, an overview, J. Geophys. Res., 124, 3724–3736, 2019.

Greatbatch, R. J.: A note on the representation of steric sea level in models that conserve volume rather than mass, J. Geophys. Res., 99, 12767–12771, 1994.

Greene, C. A., Thirumalai, K., Kearney, K. A., Delgado, J. M., Schwanghart, W., Wolfenbarger, N. S., Thyng, K. M., Gwyther, D. E., Gardner, A. S., and Blankenship, D. D.: The climate data toolbox for MATLAB, Geochem. Geophy. Geosy., 20, 3774–3781, 2019.

Hughes, T. M., Weaver, A. J., and Godfrey, J. S.: Thermohaline forcing of the Indian Ocean by the Pacific Ocean, Deep-Sea Res., 39, 965–995, 1992.

IPCC: Climate Change 2021: The Physical Science Basis, in: Contribution of Working Group I to the Sixth Assessment Report of the Intergovernmental Panel on Climate Change, edited by: Masson-Delmotte, V., Zhai, P., Pirani, A., Connors, S. L., Péan, C., Berger, S., Caud, N., Chen, Y., Goldfarb, L., Gomis, M. I., Huang, M., Leitzell, K., Lonnoy, E., Matthews, J. B. R., Maycock, T. K., Waterfield, T., Yelekçi, O., Yu, R., and Zhou, B., Cambridge University Press, in press, 2021.

Jin, X., Kwon, Y., Ummenhofer, C. C., Seo, H., Schwarzkopf, F. U., Biastoch, A., Böning, C. W., and Wright, J. S.: Influences of Pacific Climate Variability on Decadal Subsurface Ocean Heat Content Variations in the Indian Ocean, J. Climate, 31, 4157–4174, 2018.

Jyoti, J., Swapna, P., Krishnan, R., and Naidu, C. V.: Pacific modulation of accelerated south Indian Ocean sea level rise during the early 21st Century, Clim. Dynam., 53, 4413–4432, 2019.

Lee, S.-K., Park, W., Baringer, M. O., Gordon, A. L., Huber, B., and Liu, Y.: Pacific origin of the abrupt increase in Indian Ocean heat content during the warming hiatus, Nat. Geosci., 8, 445–449, 2015.

Lee, T., Fukumori, I., Menemenlis, D., Xing, Z., and Fu, L. L.: Effects of the Indonesian Throughflow on the Pacific and Indian Oceans, J. Phys. Oceanogr., 32, 1404–1429, 2002.

Levitus, S., Antonov, J., and Boyer, T.: Warming of the world ocean, 1955–2003, Geophys. Res. Lett., 32, L02604, https://doi.org/10.1029/2004GL021592, 2005.

Levitus, S., Antonov., J. I., Boyer, T. P., Baranova, O. K., Garcia, H. E., Locarnini, R. A., Mishonov, A. V., Reagan, J. R., Seidov, D., Yarosh, E. S., and Zweng, M. M.: World ocean heat content and thermosteric sea level change (0–2000 m), 1995–2010, Geophys. Res. Lett., 39, L10603, https://doi.org/10.1029/2012GL051106, 2012.

Lu, B., Ren, H.-L., Scaife, A. A., Wu, J., Dunstone, N., Smith, D., Wan, J., Eade, R., Lachlan, C. M., and Gordon, M.: An extreme negative Indian Ocean Dipole event in 2016: Dynamics and predictability, Clim. Dynam., 51, 89–100, 2018.

Marshall, G. J.: Trends in the Southern Annular Mode from observations and reanalyses, J. Climate, 16, 4134–4143, https://doi.org/10.1175/1520-0442(2003)016<4134:TITSAM>2.0.CO;2, 2003 (data available at: http://www.nerc-bas.ac.uk/icd/gjma/sam.html, last access: 5 February 2022).

Marshall, J., Jones, H., and Hill, C.: Efficient ocean modeling using non-hydrostatic algorithms, J. Marine Syst., 18, 115–134, 1998.

Masumoto, Y. and Meyers, G.: Forced Rossby waves in the southern tropical Indian Ocean, J. Geophys. Res., 103, 27589–27602, 1998.

Menemenlis, D., Fukumori, I., and Lee, T.: Using Green's functions to calibrate an ocean general circulation model, Mon. Weather Rev., 133, 1224–1240, 2005.

Menezes, V. V. and Vianna, M. L.: Quasi-biennial Rossby and Kelvin waves in the South Indian Ocean: Tropical and subtropical modes and the Indian Ocean Dipole, Deep-Sea Res., 166, 43–63, 2019.

Meyers, G.: Variation of Indonesian Throughflow and the El-Niño-Southern Oscillation, J. Geophys. Res., 101, 12255–12263, 1996.

Molcard, R., Fieux, M., and Ilahude, A. G.: The Indo-Pacific throughflow in the Timor Passage, J. Geophys. Res., 101, 12411–12420, 1996.

Monahan, A. H., Fyfe, J. C., Ambaum, M. H. P., Stephenson, D. B., and North, G. R.: Empirical Orthogonal Functions: The Medium is the Message, J. Climate, 22, 6501–6514, 2009.

Morrow, R. and Birol, F.: Variability in the southeast Indian Ocean from altimetry: Forcing mechanisms for the Leeuwin Current, J. Geophys. Res., 103, 18529–18544, 1998.

Nagura, M.: Variability in meridional transport of the subtropical circulation in the south Indian Ocean for the period from 2006 to 2017, J. Geophys. Res., 124, e2019JC015874, https://doi.org/10.1029/2019JC015874, 2020.

Nagura, M. and McPhaden, M. J.: Interannual variability in sea surface height at southern mid-latitudes of the Indian Ocean, J. Phys. Oceanogr., 51, 1595–1609, 2021.

Nieves, V., Willis, J. K., and Patzert, W. C.: Recent hiatus caused by decadal shift in Indo-Pacific heating, Science, 349, 532–535, 2015.

Oliver, E. C., Donat, M. G., Burrows, M. T., Moore, P. J., Smale, D. A., Alexander, L. V., Benthuysen, J. A., Feng, M., Sen Gupta, A., Hobday, A. J., Holbrook, N. J., Perkins-Kirkpatrick, S. E., Scannell, H. A., Straub, S. C., and Wernberg, T.: Longer and more frequent marine heatwaves over the past century, Nature commun., 9, 1–12, 2018.

Pujiana, K. and McPhaden, M. J.: Intraseasonal Kelvin Waves in the Equatorial Indian Ocean and their Propagation into the Indonesian Seas, J. Geophys. Res.-Oceans, 125, e2019JC015839, https://doi.org/10.1029/2019JC015839 2020.

Pujiana, K., Gordon, A. L., and Sprintall, J.: Intraseasonal Kelvin wave in Makassar Strait, J. Geophys. Res.-Oceans, 118, 2023–2034, 2013.

Pujiana, K., McPhaden, M. J., Gordon, A. L., and Napitu, A. M.: Unprecedented response of Indonesian Throughflow to anomalous Indo-Pacific climatic forcing in 2016, J. Geophys. Res., 124, 3737–3754, 2019.

Qiu, B.: Large-scale variability in the midlatitude subtropical and subpolar North Pacific Ocean: Observations and causes, J. Phys. Oceanogr., 32, 353–375, 2002.

Redi, M. H.: Oceanic isopycnal mixing by coordinate rotation, J. Phys. Oceanogr., 12, 1154–1158, 1982.

Ridgway, K. R. and Dunn, J. R.: Observational evidence for a Southern Hemisphere oceanic supergyre, Geophys. Res. Lett., 34, L13612, https://doi.org/10.1029/2007GL030392, 2007.

Roemmich, D. and Gilson, J.: The 2004–2008 mean and annual cycle of temperature, salinity, and steric height in the global ocean from the Argo Program, Oceanography, 82, 81–100, 2009.

Roemmich, D., Church, J., Gilson, J., Monselesan, D., Sutton, P., and Wijffels, S.: Unabated planetary warming and its ocean structure since 2006, Nat. Clim. Change, 5, 240–245, 2015.

Saji, N. H. and Yamagata, T.: Structure of SST and surface wind variability during Indian Ocean Dipole mode events: COADS observations, J. Climate, 16, 2735–2751, https://doi.org/10.1175/1520-0442(2003)016<2735:SOSASW>2.0.CO;2, 2003 (data available at: https://psl.noaa.gov/gcos_wgsp/Timeseries/DMI/, last access: 5 February 2022).

Schott, F. A., Xie, S.-P., and McCreary Jr., J. P.: Indian Ocean circulation and climate variability, Rev. Geophys., 47, RG1002, https://doi.org/10.1029/2007RG000245, 2009.

Sloyan, B. and Rintoul, S.: Circulation, renewal, and modification of Antarctic Mode and Intermediate Water, J. Phys. Oceanogr., 31, 1005–1030, 2001.

Song, Q. and Gordon, A. L.: Significance of the vertical profile of the Indonesian Throughflow to the Indian Ocean, Geophys. Res. Lett., 32, L16307, https://doi.org/10.1029/2004GL020360, 2004.

Song, Q., Vecchi, G. A., and Rosati, A. J.: The role of the Indonesian Throughflow in the Indo-Pacific climate variability in the GFDL coupled climate model, J. Clim., 20, 2434–2451, 2007.

Sprintall, J. and Révelard, A.: The Indonesian throughflow response to Indo-Pacific climate variability, J. Geophys. Res., 119, 1161–1175, 2014.

Sprintall, J., Wijffels, S. E., Molcard, R., and Jaya, I.: Direct estimates of the Indonesian Throughflow entering the Indian Ocean: 2004–2006, J. Geophys. Res., 114, C07001, https://doi.org/10.1029/2008JC005257, 2009.

Sprintall, J., Gordon, A. L., Koch-Larrouy, A., Lee, T., Potemra, J. T., Pujiana, K., and Wijffels, S. E.: The Indonesian seas and their role in the coupled ocean-climate system, Nat. Geosci., 7, 487–492, 2014.

Syamsudin, F., Kaneko, A., and Haidvogel, D. B.: Numerical and observational estimates of Indian Ocean Kelvin wave intrusion into Lombok Strait, Geophys. Res. Lett., 31, L24307, https://doi.org/10.1029/2004GL021227, 2004.

Talley, L. D.: Freshwater transport estimates and the global overturning circulation: Shallow, deep and throughflow components, Prog. Oceanogr., 78, 257–303, 2008.

Thompson, R. O. R. Y.: Observations of the Leeuwin current off Western Australia, J. Phys. Oceanogr., 14, 623–628, 1984.

Ummenhofer, C. C., Ryan, S., England, M. H., Scheinert, M., Wagner, P., Biastoch, A., and Böning, C. W.: Late 20th Century Indian Ocean Heat Content Gain Masked by Wind Forcing, Geophys. Res. Lett., 47, e2020GL088692, https://doi.org/10.1029/2020GL088692, 2020.

Valsala, V. and Ikeda, M.: Pathways and Effects of the Indonesian Throughflow Water in the Indian Ocean Using Particle Trajectory and Tracers in an OGCM, J. Climate, 20, 2994–3017, 2007.

Venugopal, T., Ali, M . M., Bourassa, M. A., Zheng, Y., Goni, G. J., Foltz, G. R., and Rajeevan, M.: Statistical evidence for the role of southwestern Indian Ocean heat content in the Indian Summer Monsoon Rainfall, Sci. Rep., 8, 1–10, https://doi.org/10.1038/s41598-018-30552-0, 2018.

Volkov, D. L., Lee, S. K., Landerer, F. W., and Lumpkin, R.: Decade-long deep-ocean warming detected in the subtropical South Pacific, Geophys. Res. Lett., 44, 927–936, 2017.

Volkov, D. L., Lee, S. K., Gordon, A. L., and Rudko, M.: Unprecedented reduction and quick recovery of the South Indian Ocean heat content and sea level in 2014–2018, Sci. Adv., 6, eabc1151, https://doi.org/10.1126/sciadv.abc1151, 2020.

Wajsowicz, R. C. and Schneider, E. K.: The Indonesian Throughflow's effect on global climate determined from the COLA Coupled Climate System, J. Climate, 14, 3029–3042, 2001.

Wang, C.: Three-ocean interactions and climate variability: a review and perspective, Clim. Dyn., 53, 5119–5136, 2019.

Wijffels, S. and Meyers, G.: An Intersection of Oceanic Waveguides: Variability in the Indonesian Throughflow Region, J. Phys. Oceanogr., 34, 1232–1253, 2004.

Wunsch, C. and Heimbach, P.: Practical global ocean state estimation, Physica D, 230, 197–208, 2007.

Wunsch, C. and Heimbach, P.: Dynamically and kinematically consistent global ocean circulation and ice state estimates, in: Ocean Circulation and Climate: A 21st Century Perspective, Chapter 21, edited by: Siedler, G., Church, J., Gould, J., and Griffies, S., Elsevier, 553–579, https://doi.org/10.1016/b978-0-12-391851-2.00021-0, 2013.

Wunsch, C., Heimbach, P., Ponte, R., and Fukumori, I.: The global general circulation of the ocean estimated by the ECCO-Consortium, Oceanography, 22, 88–103, 2009.

Wyrtki, K.: Indonesian Throughflow and the associated pressure gradient, J. Geophys. Res., 92, 12941–12946, 1987.

Xie, S.-P., Annamalai, H., Schott, F. A., and McCreary, J. P.: Structure and mechanisms of south Indian Ocean climate variability, J. Climate, 15, 864–878, 2002.

Yuan, D., Hu, X., Xu, P., Zhao, X., Masumoto, Y., and Han, W.: The IOD-ENSO precursory teleconnection over the tropical Indo-Pacific Ocean: dynamics and long-term trends under global warming, J. Ocean. Limnol., 36, 4–19, 2018.

Yuan, X., Ummenhofer, C. C., Seo, H., and Su, Z.: Relative contributions of heat flux and wind stress on the spatiotemporal upper-ocean variability in the tropical Indian Ocean, Environ. Res. Lett., 15, 084047, https://doi.org/10.1088/1748-9326/ab9f7f, 2020.

Zhang, H., Menemenlis, D., and Fenty, I. G.: ECCO LLC270 ocean-ice state estimate, MIT Libraries, https://doi.org/1721.1/119821, 2018 (data available at: https://ecco.jpl.nasa.gov/drive/files/Version5/Alpha, last access: 8 February 2022, login required).

Zhang, Y., Feng, M., Du, Y., Phillips, H. E., Bindoff, N. L., and McPhaden, M. J.: Strengthened Indonesian Throughflow drives decadal warming in the Southern Indian Ocean, Geophys. Res. Lett., 45, 6167–6175, 2018.

Zhang, T., Hoell, A., Perlwitz, J., Eischeid, J., Murray, D., Hoerling, M., and Hamill, T. M.: Towards Probabilistic Multivariate ENSO Monitoring, Geophys. Res. Lett., 46, https://doi.org/10.1029/2019GL083946, 2019 (data available at: https://psl.noaa.gov/enso/mei/, last access: 8 February 2022).

Zheng, C. W., Li, C. Y., and Pan, J.: Propagation route and speed of swell in the Indian Ocean, J. Geophys. Res., 123, 8–21, 2018.

Zhuang, W., Feng, M., Du, Y., Schiller, A., and Wang, D.: Low-frequency sea level variability in the southern Indian Ocean and its impacts on the oceanic meridional transports, J. Geophys. Res., 118, 1302–1315, 2013.